Photothermal nanozymes to self-augment combination cancer therapy by dual-glutathione depletion and hyperthermia/acidity-activated hydroxyl radical generation

Tzu-Hao Wang [a], Ming-Yen Shen [a], Nien-Tzu Yeh [a], Yu-Hsin Chen [a], Tsai-Ching Hsu [b,c,d], Hao-Yang Chin [b], Yi-Ting Wu [b], Bor-Show Tzang [b,c,d,e,*], Wen-Hsuan Chiang [a,*]

[a] Department of Chemical Engineering, National Chung Hsing University, Taichung 402, Taiwan
[b] Institute of Medicine, Chung Shan Medical University, Taichung 402, Taiwan
[c] Immunology Research Center, Chung Shan Medical University, Taichung 402, Taiwan
[d] Clinical Laboratory, Chung Shan Medical University Hospital, Taichung 402, Taiwan
[e] Department of Biochemistry, School of Medicine, Chung Shan Medical University, Taichung 402, Taiwan

G R A P H I C A L   A B S T R A C T
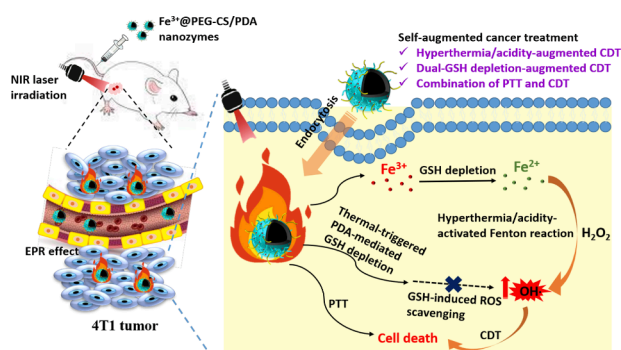
A R T I C L E   I N F O

A B S T R A C T

Chemodynamic therapy (CDT) has emerged as a promising strategy for tumor treatment. Nevertheless, the low Fenton catalytic efficiency and the high concentration of glutathione (GSH) in cancer cells largely decline antitumor efficacy of CDT. To self-augment antitumor effect of the CDT by combining with photothermal therapy (PTT), the unique photothermal nanozymes that doubly depleted GSH, and generated massive hydroxyl radicals (·OH) in the hyperthermia/acidity-activated manner were developed. Through the coordination of Fe^{3+} ions with PEGylated chitosan (PEG-CS)-modified polydopamine (PDA) nanoparticles, the attained Fe^{3+}@PEG-CS/PDA nanozymes showed outstanding colloidal stability, photothermal conversion efficiency and acidity-triggered Fe^{3+} release. By GSH-mediated valence states transition of Fe^{3+} ions and Michael reaction between GSH and quinone-rich PDA, the nanozymes sufficiently executed dual depletion of GSH with the elevated temperature. Under mimic tumor acidity and near-infrared (NIR) irradiation condition, the endocytosed nanozymes effectively converted intracellular H_2O_2 into toxic ·OH upon amplified Fenton reaction, thereby potently killing 4T1 cancer

cells and RAW 264.7 cells. Importantly, the nanozymes prominently suppressed 4T1 tumor growth in vivo and metastasis of cancer cells by CDT/PTT combination therapy without significant systemic toxicity. Our study provides novel visions in design of therapeutic nanozymes with great clinical translational prospect for tumor treatment.

1. Introduction

Chemodynamic therapy (CDT), an emerging cancer treatment modality, was first reported by Shi and co-workers in 2016.[1] CDT uses multivalent metal elements (e.g., $Fe^{2+/3+}$, $Ce^{3+/4+}$, $Cu^{1+/2+}$, $Mn^{2+/4+}$, etc.) to catalyze hydrogen peroxide (H_2O_2) via Fenton or Fenton-like reactions to generate toxic hydroxy radical ($\cdot OH$), as a kind of common reactive oxygen species (ROS), within the tumor sites, thus evoking oxidative damage of cancer cells [1–8]. CDT shows the great potential in clinical cancer treatment due to its several advantages including (1) generation of $\cdot OH$ without light irradiation or oxygen consumption, (2) low side effect and treatment cost, and (3) tumor microenvironment sensitivity [9–10]. Nevertheless, redox homeostasis, as a cellular inherent defense mechanism, largely declines the CDT-mediated anticancer efficacy by keeping the balance of oxidant and antioxidant [11–14]. Glutathione (GSH), as a main intracellular antioxidant, can remarkably reduce intracellular ROS levels to prevent ROS-elicited oxidative injury, thus leading to resistance to ROS-involved cancer therapy [11–14]. Furthermore, the low intracellular concentration of endogenous H_2O_2 is another hurdle impairing the anticancer potency of CDT [12,15–17]. To address these issues, increasing studies utilized the strategies of depleting intracellular GSH and rising H_2O_2 levels to amplify the ROS-elicited oxidative damage of cancer cells [18–21]. For example, Lin et al. developed a self-reinforcing MnO_2-based nanoagent with Fenton-like Mn^{2+} delivery and GSH depletion properties to enhance CDT [18]. In addition, Huang's group utilized poly(ethylene glycol) (PEG)-modified glucose oxidase (GOx) as a template to fabricate biodegradable copper-doped calcium phosphate nanoparticles for delivery of doxorubicin (DOX). As an enzyme catalyst, GOx efficiently catalyze intracellular glucose to generate H_2O_2, thus not only starving cancer cells, but also supplying H_2O_2 for subsequent Fenton-like reaction [20]. Also, the redox reaction between the released Cu^{2+} ions and intracellular GSH not only consumed GSH but also reduced Cu^{2+} to Cu^+ ions, and then decomposed H_2O_2 to produce $\cdot OH$ by a Cu^+-mediated Fenton-like reaction, thus augmenting CDT efficacy.

Despite significant progress, it is still challenging for single CDT to effectively suppress tumor growth and metastasis [22–24]. Recently, to enhance the antitumor effects of CDT by changing their focus from a single CDT to CDT-involved combination therapies, various combination therapy modalities including CDT/photothermal therapy (PTT) [23–27], CDT/photodynamic therapy (PDT) [28,29], CDT/chemotherapy [20,30,31], CDT/starving therapy [32,33] and CDT/immunotherapy [34,35] have been developed. Among them, due to minimal invasiveness, high spatiotemporal selectivity and oxygen independence of PTT, and the accelerated Fenton reaction rate of CDT in the assist of hyperthermia, the combination of CDT and PTT has been considered as a highly effective and comparatively safe modality [9,36,37]. For instance, Tang's group fabricated a Cu^{2+}-doped mesoporous polydopamine (PDA) decorated with hyaluronic acid (HA) (CuPDA@HA) nanoparticles as β-Lapachone (Lapa) carrier for CDT-sensitized low-temperature PTT [23]. The CuPDA@HA nanoparticles not only catalyzed H_2O_2 self-sufficient Fenton reaction and diminished the intratumoral GSH, but also enhanced the photothermal conversion effect of PDA. The Lapa-loaded CuPDA@HA nanoparticles also promoted the intracellular H_2O_2 generation to boost CDT. Under low-power NIR irradiation, the Lapa-carrying CuPDA@HA nanoparticles remarkably killed cancer cells both in vitro and in vivo. Furthermore, as reported by Lu et al. [25], the activatable nanozyme-mediated 2,2′-azino-bis (3-ethylbenzothiazoline-6-sulfonic acid) (ABTS)-loaded ABTS@MIL-100/

poly(vinylpyrrolidine) (AMP) nanoreactors (NRs) were developed for imaging-guided combined tumor PTT/CDT. The attained AMP NRs were selectively activated by the tumor microenvironment through a nanozyme-mediated "two-step rocket-launching-like" procedure to provoke its photoacoustic imaging signal and PTT ability. Also, the AMP NRs appreciably enhanced CDT by simultaneously generating $\cdot OH$ in response to the high H_2O_2 level of the tumor microenvironment and depleting intracellular GSH, thus prominently boosting antitumor potency in combination with PTT. Although a varied of multifunctional nanoplatforms have been successfully created to realize the combination of CDT and PTT for cancer treatment [23–25,38], the strategies adopted to prepare these nanoparticles often involved the use of non-biocompatible and complicated materials or multiple-step approaches, thus being not beneficial to clinical application. Besides, for most of enzyme-like nanoparticles, the redox reaction between the Fenton metal ions and intracellular GSH molecules only results in limited depletion of intracellular GSH, thus being incapable to sufficiently disrupt the cellular redox homeostasis and elevate intracellular ROS level.

To overcome the aforementioned problems, a practical tactic was developed herein to fabricate multifunctional PDA-based nanozymes capable of potently depleting GSH, decomposing H_2O_2 to produce $\cdot OH$ and converting NIR light into heat for boosting antitumor effect by the combined CDT and PTT (Scheme 1). Several studies showed that the melanin-like PDA exhibited several advantages including excellent biocompatibility, high photothermal conversion capability, strong metal-ion chelation [3,39,40]. Also, PDA has been demonstrated to considerably deplete endogenous GSH, and self-supply H_2O_2 by providing electrons to oxygen [12,41,42]. Therefore, in this study, the photothermal PDA nanoparticles from oxidative self-polymerization of dopamine (DA) molecules were not only utilized as vehicles to deliver ferric ions (Fe^{3+}) into cancer cells, but also used as GSH scavenger to self-augment the CDT and PTT combination therapy. To promote colloidal stability of PDA nanoparticles in serum-containing milieu of physiological salt concentration, the hydrophilic and biocompatible PEGylated chitosan (PEG-CS) conjugates were synthesized and then chemically decorated on the surfaces of PDA nanoparticles upon Michael addition between primary amine groups of PEG-CS and 5,6-dihydroxyindole (DHI) moieties of PDA. Finally, through the coordination of Fe^{3+} ions with catechol groups of PEG-CS/PDA nanoparticles, the Fe^{3+}@PEG-CS/PDA nanozymes were obtained. The Fe^{3+}@PEG-CS/PDA nanozymes showed not only outstanding photothermal conversion efficiency and robust photothermal stability but also acidity-triggered Fe^{3+} release. Notably, the nanozymes not only reacted with GSH to elicit GSH consumption and generate Fe^{2+} but also displayed thermal/acidity-enhanced Fe^{2+}/Fe^{3+}-mediated cascade Fenton reaction, thereby effectively decomposing H_2O_2 into $\cdot OH$. Also, a large amount of the quinone moieties from PDA of nanozymes irreversibly reacted with thiols by Michael addition reaction, thus considerably depleting GSH. Importantly, under mimic tumor acidity and NIR irradiation condition, the endocytosed Fe^{3+}@PEG-CS/PDA nanozymes remarkably decomposed intracellular H_2O_2 to generate $\cdot OH$ upon hyperthermia/acidity-amplified Fenton reaction, thereby effectively killing 4T1 mouse breast cancer cells and murine macrophages-like RAW 264.7 cells. By the combination of CDT and PTT, the nanozymes not only significantly inhibited 4T1 breast tumor growth in vivo without appreciable systemic toxicity, but also potently reduced the metastasis of cancer cells to major organs.
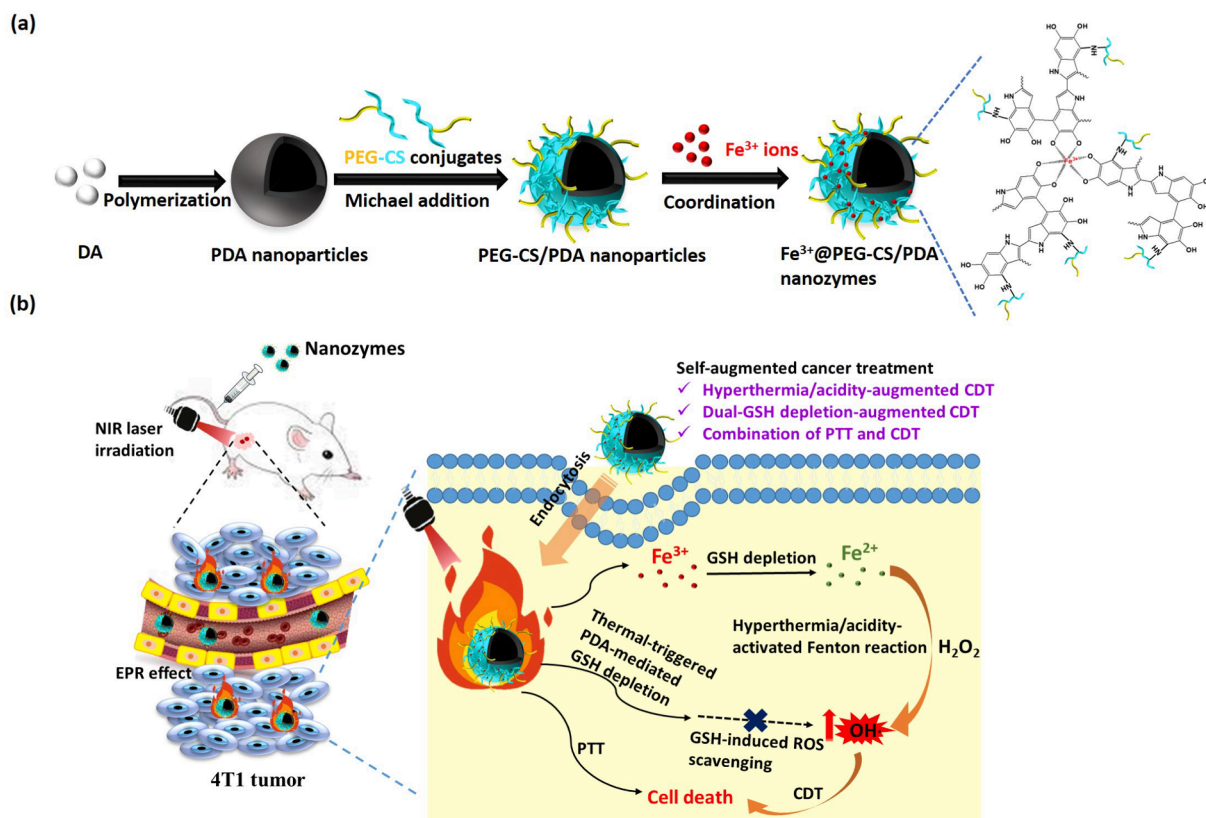
Scheme 1. Schematic illustration of (a) fabrication of Fe^{3+}@PEG-CS/PDA nanozymes and (b) their antitumor effect by the CDT/PTT combination therapy.

2. Experimental section

2.1. Materials and reagents

Chitosan oligosaccharide (MW 5.0 kDa, 81 % degree of deacetylation) was obtained from Glentham Life Science Ltd. (UK). Methoxy poly (ethylene glycol) (mPEG) (MW 5.0 kDa), 3-(4,5-Dimethylthiazol-2-yl)-2,5-diphenyltetrazolium bromide (MTT), methylene blue solution (MB, 5 mg/mL), 2′,7′-Dichlorodihydrofluorescein diacetate (DCFH-DA), RPMI-1640 medium, and D_2O (99.9 atom % D) were purchased from Sigma-Aldrich (USA). N-(3-Dimethylaminopropyl)-N'-ethyl-carbodiimide hydrochloride (EDC, 95 %) was attained from Matrix Scientific (USA). Pierce® RIPA buffer and 1,10-phenanthroline monohydrate (Phe, ≥99.5%) were attained from Thermo Fisher Scientific. Dopamine hydrochloride (DA), N-hydroxysuccinimide (NHS, 98%) and succinic anhydride (99%) were acquired from Alfa Aesar (USA). Indocyanine green (ICG, 95.4%) was purchased from Chem-Impex International (USA). ABTS (95%) was obtained from Combi-Blocks (USA). GSH assay kit was purchased from Elabscience (USA). 5,5′-dithiobis (2-nitrobenzoic acid) (DTNB, 99%) was purchased from Fluorochem (UK). Fetal bovine serum (FBS) was purchased from Hyclone (USA). Hoechst 33,342 was purchased from Invitrogen. Anti-Ki67 antibodies (ab15580) was obtained from Abcam. Deionized water was produced from Milli-Q Synthesis (18 MΩ, Millipore). All other chemicals were reagent grade and used as received. 4T1 cells (murine breast cancer cell line), RAW 264.7 cells and WS1 cells (human skin fibroblast cells) were acquired from Food Industry Research and Development Institute (Hsinchu City, Taiwan).

2.2. Synthesis and characterization of PEG-CS conjugates

According to our previous work [43], the mPEG-COOH employed in this study was attained upon the ring-opening reaction of succinic anhydride with mPEG. To obtain the PEG-CS conjugates (degree substitution (DS): 8.44), the EDC/NHS-mediated amidation of chitosan and mPEG-COOH was conducted (Fig. S1). In brief, chitosan (100 mg), mPEG-COOH (295 mg) and NHS (136 mg) were dissolved in deionized water (4.0 mL), followed by the addition of EDC (227 mg) under stirring. The mixture was stirred at 25 °C for 48 h and dialyzed (Cellu Sep MWCO 6000 ~ 8000) against deionized water to eliminate NHS and EDC, followed by freeze drying to obtain the product. Fourier transform infrared (FT-IR) measurements of mPEG-COOH, chitosan and PEG-CS were performed on a FT-720 spectroscopy (HORIBA, Japan) using KBr pellet for the sample preparation. The DS of chitosan with mPEG-COOH defined as the number of mPEG segments per 100 glucosamine units was determined by proton nuclear magnetic resonance (^{1}H NMR) characterization (Agilent DD2 600 MHz NMR spectrometer) using D_2O as the solvent at 25 °C. For comparison, the PEG-CS conjugates with different DS values were synthesized by the similar approach.

2.3. Preparation of Fe^{3+}@PEG-CS/PDA nanozymes

Through the oxidative self-polymerization of DA under alkaline conditions, the PDA nanoparticles used in this study were synthesized according to a previously reported method [44]. Briefly, 150 μL of NaOH solution (1 N) was added to 20 mL of DA solution (1.79 mg/mL) and gently stirred at 50 °C for 5 h, followed by dialysis (Cellu Sep MWCO 6000 ~ 8000) with pH 8.0 phosphate buffer at 4 °C to eliminate unreacted DA. To attain the PEG-CS/PDA nanoparticles with different amounts of PEG-CS adducts on the surfaces of PDA nanoparticles, the PEG-CS conjugates with DS of 8.44 (0.25, 0.5, 1.0 and 1.5 folds with respect to weight of PDA nanoparticles in feed) were dissolved in 0.1 mL pH 8.0 phosphate buffer, followed by dropwise addition of 0.9 mL PDA nanoparticle solution (1.1 mg/mL) under stirring. The mixture solution was stirred at 25 °C for 24 h and dialyzed (Cellu Sep MWCO 12000 ~ 14000) against pH 8.0 phosphate buffer at 4 °C for overnight. For
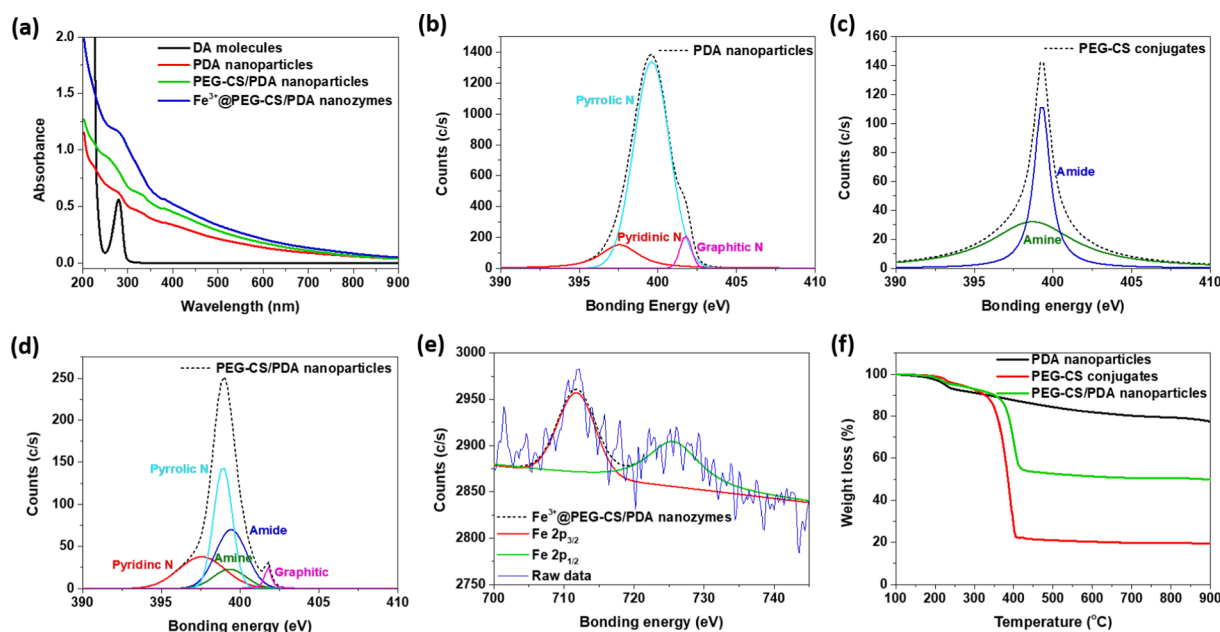
Fig. 1. (a) UV/Vis spectra of DA molecules, PDA nanoparticles, PEG-CS/PDA nanoparticles and Fe^{3+}@PEG-CS/PDA nanozymes in aqueous solution. XPS spectra of (b) PDA nanoparticles, (c) PEG-CS conjugates, (d) PEG-CS/PDA nanoparticles and (e) Fe^{3+}@PEG-CS/PDA nanozymes. (f) TGA profiles of PDA nanoparticles, PEG-CS conjugates and PEG-CS/PDA nanoparticles.

comparison, the PEG-CS conjugates of different DS values were used to decorate PDA nanoparticles in a similar manner. For preparation of Fe^{3+}@PEG-CS/PDA nanozymes, 0.1 mL of PEG-CS (DS: 8.44) conjugate solution (15 mg/mL) was added dropwise into 0.85 mL of PDA nanoparticle solution (1.2 mg/mL) under stirring. After 1 h, 50 μL ferric chloride (0.09 M) solution was added dropwise into the mixture solution and then stirred at 25 °C for additional 23 h. Next, the resulting solution was dialyzed (Cellu Sep MWCO 12000 ~ 14000) against pH 8.0 phosphate buffer at 4 °C for 24 h to remove unloaded ferric ions, and the purified nanozymes were attained.

2.4. Structural characterization

The absorption spectra of DA molecules and PDA-based nanoparticles in pH 7.4 phosphate buffer were obtained using a UV/Vis spectrophotometer (V-730, JASCO, Japan). X-ray photoelectron spectroscopy (XPS) analysis was performed by a PHI 5000 VersaProbe III X-ray photoelectron spectrometer (ULVAC-PHI, Japan) with AlKα radiation (hγ = 1486.6 eV) at 15 kV and 150 W. Thermogravimetric analysis (TGA) was conducted with thermogravimetric analyzer EXSTAR TG/DTA 6200 (Seiko Instruments Inc) in an N_2 atmosphere by heating the sample to 900 °C at the rate of 10 °C/min. The zeta potential of pristine PDA nanoparticles, PEG-CS/PDA nanoparticles and Fe^{3+}@PEG-CS/PDA nanozymes in aqueous solutions of different pH was determined by a Litesizer 500 (Anton Paar, USA) and their particle size and particle size distribution were measured by a Brookhaven BI-200SM goniometer equipped with a BI-9000 AT digital correlator using a solid-state laser (35 mW, λ = 637 nm). At least triplicate measurements of each sample were conducted and then averaged. In addition to angular-dependent autocorrelation functions, the ratio of the root-mean-square radius of gyration (R_g) to the mean hydrodynamic radius (R_h) of PEG-CS/PDA nanoparticles and Fe^{3+}@PEG-CS/PDA nanozymes was obtained by angular dependent dynamic and static light scattering (DLS/SLS) measurements using the aforementioned apparatus. The R_g value of PEG-CS/PDA nanoparticles and Fe^{3+}@PEG-CS/PDA nanozymes in pH 7.4 0.15 M phosphate buffered saline (PBS) was quantitatively determined using the Berry plot of the scattering intensity ($I_{ex}^{1/2}$) versus the square of the scattering vector (q^2) from the angle-dependent measurements of the

light scattering intensity. The morphology of various PDA-based nanoparticles was attained by scanning electron microscope (SEM) (JEOL JSM-7800F Prime Schottky Field Emission SEM, Japan, an acceleration voltage of 3 kV) and transmission electron microscope (TEM) (HT7700, Hitachi, Japan). The SEM samples were prepared by sputter coating of PDA-based nanoparticles with platinum, while the TEM samples were obtained by placing a few drops of nanoparticle solution on a 300-mesh copper grid covered with carbon.

2.5. Determination of Fe^{3+} content

To quantify the Fe^{3+} content of Fe^{3+}@PEG-CS/PDA nanozymes, the nanozymes were diluted 20 times using HNO_3 solution (1%) and the mixture was then stirred for 24 h to completely dissociate the iron. The ferric ion concentration was quantified by inductively coupled plasma-atomic emission spectrometry (ICP-AES) with an Agilent 725 emission spectrometer.

2.6. In vitro Fe^{3+} release from Fe^{3+}@PEG-CS/PDA nanozymes

The nanozyme solution (1.2 mL) was dialyzed (Cellu Sep MWCO 12000–14000) against PBS (pH 7.4) and acetate buffer (pH 5.0) (20 mL) at 37 °C, respectively. The internal sample (200 μL) was withdrawn periodically and then mixed with vitamin C solution (250 μL, 40 mM) for complete reduction of Fe^{3+} into Fe^{2+} ions. The resulting solution was then added into Phe solution (50 μL, 4 mM) and equilibrated at 37 °C for 30 min for formation of tangerine Fe^{2+}/Phe complexes. The absorbance of mixture solution at 512 nm was determined by a UV/Vis spectrophotometer. The cumulative Fe^{3+} release (%) was calculated by the following equation:

Cumulative Fe^{3+} release (%) = ((Initial absorbance - absorbance at the predetermined time points)/Initial absorbance) × 100%.

2.7. Photothermal conversion effect

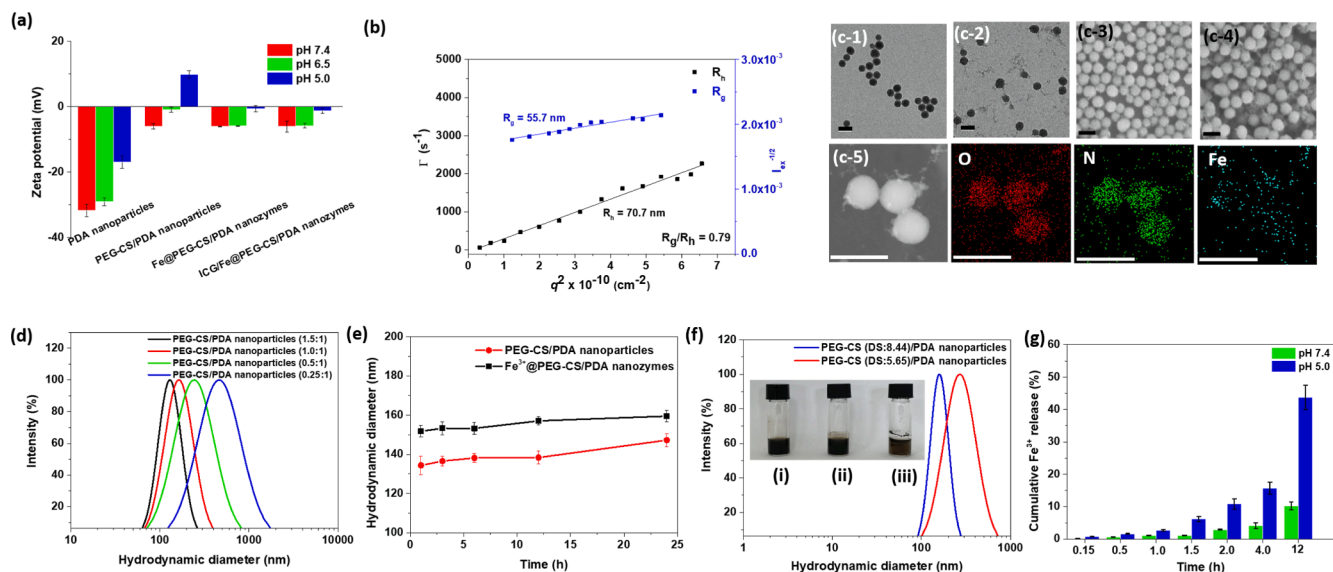PEG-CS/PDA nanoparticles and Fe^{3+}@PEG-CS/PDA nanozymes

Fig. 2. (a) Zeta potential of various PDA-based nanoformulations in aqueous solutions of pH 7.4, 6.5 and 5.0 (n = 3). (b) Berry plot for R_g and angle dependent correlation function of R_h of PEG-CS/PDA nanoparticles in pH 7.4 0.15 M PBS. TEM images of (c-1) PEG-CS/PDA nanoparticles and (c-2) Fe^{3+}@PEG-CS/PDA nanozymes. Scale bars are 200 nm. SEM images of (c-3) PEG-CS/PDA nanoparticles and (c-4) Fe^{3+}@PEG-CS/PDA nanozymes. Scale bars are 200 nm. (c-5) X-ray spectroscopy (EDS) elemental maps of Fe^{3+}@PEG-CS/PDA nanozymes. Scale bars are 250 nm. (d) DLS particle size distribution profiles of PEG-CS/PDA nanoparticles with different PEG-CS/PDA weight ratios dispersed in pH 7.4 0.15 M PBS. (e) Colloidal stability of PEG-CS/PDA nanoparticles and Fe^{3+}@PEG-CS/PDA nanozymes in pH 7.4 10 % FBS-containing RPMI medium at 37 °C (n = 3). (f) DLS particle size distribution profiles of PEG-CS (DS: 8.44)/PDA nanoparticles and PEG-CS (DS: 5.65)/ PDA nanoparticles dispersed in pH 7.4 0.15 M PBS. The photographs of (i) PEG-CS (DS: 8.44)/PDA nanoparticles, (ii) PEG-CS (DS: 5.65)/PDA nanoparticles and (iii) PEG-CS (DS: 4.41)/PDA nanoparticles in pH 7.4 0.15 M PBS are also included. (g) Cumulative Fe^{3+} release profiles of Fe^{3+}@PEG-CS/PDA nanozymes at pH 7.4 and 5.0 at 37 °C (n = 3).

dispersed in pH 7.4 PBS (1.0 mL), respectively, were irradiated by 808 nm near-infrared (NIR) laser with different power densities (0.5, 0.75, 1.0 and 1.25 W/cm^2) for 5 min. The solution temperatures and infrared thermographic maps were recorded with an infrared thermal imaging camera (Thermo Shot F20, NEC Avio Infrared Technologies, Germany). Moreover, the temperature elevation of an aqueous dispersion of Fe^{3+}@PEG-CS/PDA nanozymes with different concentrations (25 ∼ 200 μg/mL) exposed to laser irradiation (1.0 W/cm^2) for 5 min was determined by the above apparatus. The photothermal stability of PEG-CS/PDA nanoparticles and Fe^{3+}@PEG-CS/PDA nanozymes (200 μg/mL) was assessed by heating with 808 nm laser irradiation (1.0 W/cm^2) for 5 min and then cooling to room temperature. The heating–cooling cycle was repeated three times. The photothermal conversion efficiency was calculated according to the following formula [45].

$$\eta = \frac{hA(\Delta T_{max,mix} - \Delta T_{max,PBS})}{I(1 - 10^{-A_\lambda})} \qquad (1)$$

where η is the photothermal conversion efficiency of PDA and BI-PC/PDA nanoparticles, *h* is the heat transfer coefficient, *A* is the surface area of the container, and ΔT_{max} is the temperature change at the maximum steady-state temperature, *I* is the laser power, A_λ is the absorbance of PDA-based nanoparticles and nanozymes at the wavelength of 808 nm in PBS.

In this equation, only *hA* is unknown. In order to obtain *hA*, the θ, which is defined as the ratio of ΔT to ΔT_{max} was introduced:

$$\theta = \frac{\Delta T}{\Delta T_{max}} \qquad (2)$$

where ΔT is the temperature change, which is defined as $T - T_{surr}$ (*T* and T_{surr} are the solution temperature and ambient temperature of the surroundings, respectively). Thus, *hA* can be determined as following:

$$hA = \frac{mC_p}{\tau_s} \qquad (3)$$

where τ_s is the slope of the linear time data from the cooling period *vs* -Lnθ, m and C_p are the mass and heat capacity of PBS, respectively.

2.8. Catalytic activity of Fe^{3+}@PEG-CS/PDA nanozymes

In order to confirm that Fe^{3+} ions of Fe^{3+}@PEG-CS/PDA nanozymes can be reduced to Fe^{2+} ions by GSH, the Phe assay was used. In brief, Fe^{3+}@PEG-CS/PDA nanozymes (100 μg/mL) were added in pH 7.4 PBS containing GSH (10 mM) and Phe (0.2 mM), and incubated at 37 °C for 2 h. The absorption spectrum of mixture solution was attained by a UV/Vis spectrophotometer. For comparison, the experiment was also performed using the following groups: Fe^{3+}@PEG-CS/PDA nanozymes in the lack of GSH, PEG-CS/PDA nanoparticles in the presence of GSH and GSH alone. Moreover, the catalytic activity (·OH generation) of Fe^{3+}@PEG-CS/PDA nanozymes at pH 5.5 and 7.4 was evaluated by determining the absorbance of MB at 665 nm due to the ·OH-triggered degradation of MB. Briefly, 10 μL of MB (10 mg/mL) solution was added into 0.19 mL of aqueous solutions of Fe^{3+}@PEG-CS/PDA nanozymes (526 μg/mL) at pH 5.5 and 7.4, followed by addition of 0.8 mL of H_2O_2 (0.01 M). The mixture solution was incubated in dark at 37 °C. At different time intervals, the maximum absorbance of MB was determined with a UV/Vis spectrophotometer and normalized to that at the beginning. Also, the degradation of MB by Fe^{3+}/Fe^{2+}-mediated Fenton-like reaction of nanozymes in the presence of 10 mM GSH was performed at pH 5.5 and different temperatures (25, 37 and 50 °C) for 2 h. Besides, the catalytic activity of Fe^{3+}@PEG-CS/PDA nanozymes at pH 5.0 and 7.4 was further explored by determining the absorbance of oxABTS at 425 nm due to the ·OH-elicited oxidation of ABTS. In short, the mixture solution containing 5 mM ABTS, 8 mM H_2O_2, 10 mM GSH and 100 μg Fe^{3+}@PEG-CS/PDA nanozymes at pH 7.4 and 5.5 was incubated at 37 °C for 12 h. After that, the absorption spectrum of the resulting solution was obtained by a UV/Vis spectrophotometer.
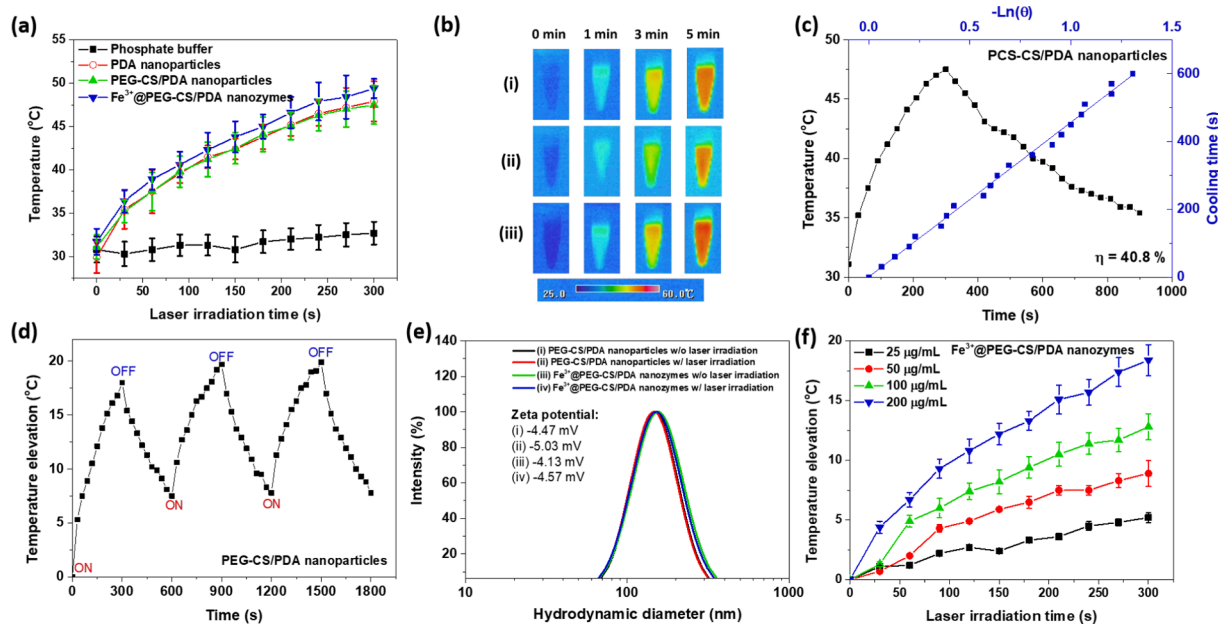
Fig. 3. (a) Temperature profiles and (b) thermal images of (i) PDA nanoparticles, (ii) PEG-CS/PDA nanoparticles and (iii) Fe^{3+}@PEG-CS/PDA nanozymes (PDA concentration: 90 µg/mL) in pH 7.4 phosphate buffer (n = 3). (c) Temperature profile of PEG-CS/PDA nanoparticle solution (concentration: 200 µg/mL) after exposure to 808 nm laser irradiation (1.0 W/cm^2) for single on/off cycle, and plot of cooling time versus negative logarithm of the temperature driving force. (d) Temperature change of each heating cycle of PEG-CS/PDA nanoparticle solution (PDA concentration: 90 µg/mL) exposed to irradiation of 808 nm NIR laser (1.0 W/cm^2). (e) DLS particle size distribution and zeta potential of PEG-CS/PDA nanoparticles and Fe^{3+}@PEG-CS/PDA nanozymes with or without NIR laser irradiation. (f) Temperature change of aqueous solutions of Fe^{3+}@PEG-CS/PDA nanozymes with different concentrations under NIR laser irradiation (n = 3).

2.9. GSH depletion capability of Fe^{3+}@PEG-CS/PDA nanozymes

The GSH depleting capability of PEG-CS/PDA nanoparticles and Fe^{3+}@PEG-CS/PDA nanozymes was studied by DTNB assay. Briefly, the PEG-CS/PDA nanoparticles (100 µg/mL) and Fe^{3+}@PEG-CS/PDA nanozymes (100 µg/mL) were respectively added to 1 mL of GSH solution (1 mM) and incubated at different temperatures (25, 37 and 50 °C) for 2 h. Next, the resulting solution was centrifugated to collect the supernatant. Then, 250 µL of DTNB (0.2 mM) was added to the supernatant and the absorbance of the mixture at 412 nm was measured.

2.10. ICG loading

To evaluate the in vitro cellular uptake and in vivo biodistribution of Fe^{3+}@PEG-CS/PDA nanozymes by fluorescence imaging, the amphiphilic fluorescent dye, ICG, was incorporated into these nanozymes. The ICG-labeled Fe^{3+}@PEG-CS/PDA nanozymes were prepared as follow. 0.1 mL of PEG-CS conjugate (DS: 8.44) solution (15 mg/mL) was added dropwise into 0.8 mL of PDA nanoparticle solution (~1.3 mg/mL) under stirring. After 1 h, 50 µL ferric chloride (0.09 M) was added dropwise into the mixture solution and then stirred at 25 °C for additional 19 h. Next, ICG dissolved in DMSO (2.0 mg/mL, 50 µL) was added dropwise into the above solution and stirred in dark at room temperature for 5 h, followed by dialysis (Cellu Sep MWCO 12000 ~ 14000) against pH 8.0 phosphate buffer at 4 °C to remove unloaded ICG molecules and DMSO. To quantify ICG encapsulated within hybrid nanoparticles, a prescribed volume of ICG-encapsulated nanoparticle solution was lyophilized and then dissolved in DMSO to extract the drug. The absorbance of ICG at 794 nm was determined by a UV/Vis spectrophotometer (U-2900, Hitachi).

2.11. In vitro cellular uptake, intracellular GSH consumption and ROS generation

4T1 cells (2 × 10^5 cells/well) seeded onto 22 mm round glass coverslips in 6-well plates were incubated with free ICG molecules and ICG-labeled Fe^{3+}@PEG-CS/PDA nanozymes (ICG concentration = 5 µM), respectively, at 37 °C for 1 and 4 h. After being washed twice with Hanks' balanced salt solution (HBSS) and immobilized with 4 % formaldehyde, cell nuclei were stained with Hoechst 33342. The cellular images were attained using a CLSM (Olympus, FluoView FV3000, Japan) at the excitation wavelengths of 405 and 782 nm for Hoechst and ICG, respectively. Furthermore, the cellular uptake of free ICG molecules and ICG-labeled nanozymes (ICG concentration = 5 µM) by 4T1 cells at 37 °C was evaluated by FACSCalibur flow cytometer (BD Bioscience). After 1 and 4 h incubation and detachment with trypsin-EDTA solution, the treated 4T1 cells (2 × 10^5 cells/well) were suspended in PBS (1.0 mL). The ICG fluorescence of a minimum of 1 × 10^4 cells per batch was analyzed by plotting fluorescence intensity on a four-decade log scale.

To evaluate intracellular GSH consumption, 4T1 cells (1x10^5/well) seeded in 6-well plate were incubated with PEG-CS/PDA nanoparticles and Fe^{3+}@PEG-CS/PDA nanozymes (200 µg/mL), respectively, for 24 h. Then, cells were washed twice with PBS and detached with trypsin-EDTA, followed by centrifugation (1500 rpm) for 5 min. The collected cell pellets were irradiated by 808 nm NIR laser (1.25 W/cm^2) for 5 min. The treated cells were dispersed in 0.5 mL RIPA buffer and frozen and thawed for cell lysis. After being centrifuged at 12000 rpm for 10 min at 25 °C, the supernatant was acquired and intracellular GSH level of each group was determined by DTNB-thiol assay kit through a microplate reader at a wavelength of 405 nm. The intracellular GSH level of 4T1 cells treated with PEG-CS/PDA nanoparticles or Fe^{3+}@PEG-CS/PDA nanozymes without laser irradiation was also evaluated in a similar manner.

On the other hand, the ROS generation in 4T1 cells incubated with PEG-CS/PDA nanoparticles or Fe^{3+}@PEG-CS/PDA nanozymes (100 µg/mL) for 24 h, irradiated if needed (808 nm, 1 W/cm^2, 3 min) was studied using DCFH-DA assay. 4T1 cells seeded in 6-well plates at 2 × 10^5 cells/well were incubated with PEG-CS/PDA nanoparticles or Fe^{3+}@PEG-CS/PDA nanozymes at pH 7.4 or 6.5 for 24 h, followed by treatment with DCFH-DA (10 µM) for 30 min. Treated cells were then irradiated by an 808-nm NIR laser for 3 min. Thirty minutes after irradiation, treated cells were washed twice with PBS. The cellular images were attained
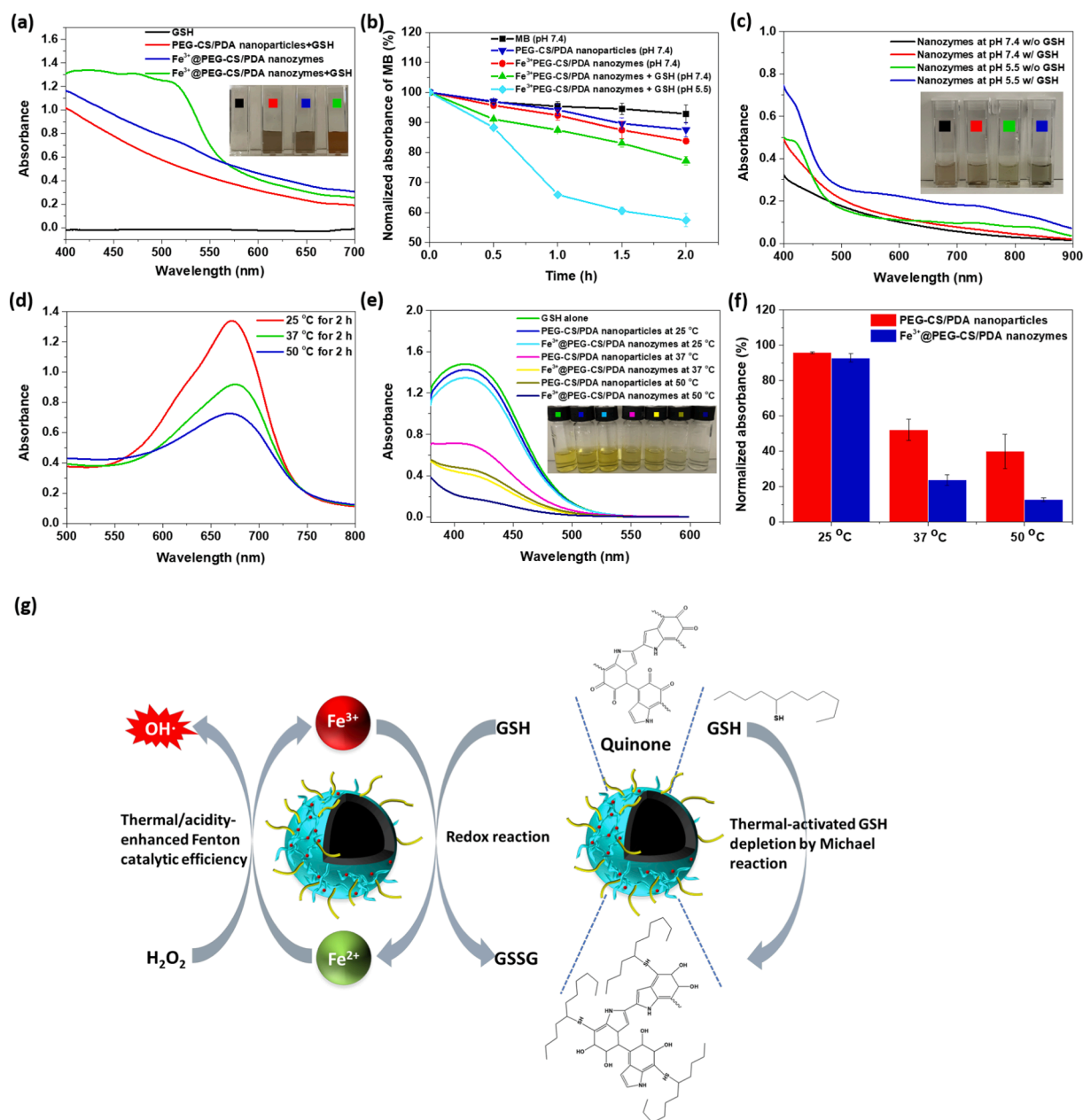
Fig. 4. Cascade catalytic reaction for ·OH generation and GSH consumption. (a) UV/Vis spectra of Phe with different treatments. Inset: photographs of the corresponding samples and the reaction of Phe with Fe^{2+} to produce tangerine complex. (b) Normalized absorbance of MB with different treatments at 37 °C (·OH generation) (n = 3). (c) UV/Vis spectra of ABTS solution with the addition of nanozymes with or without GSH at pH 7.4 and 5.0. Inset: photographs of the corresponding samples and the formation of oxidized ABTS (oxABTS) with green color. (d) UV/Vis spectra of MB treated with Fe^{3+}@PEG-CS/PDA nanozymes in the presence of GSH (10.0 mM) at pH 5.5 and at different temperatures for 2 h. (e) UV/Vis spectra of DTNB receiving various treatments for 2 h. Inset: photographs of the corresponding samples and the reaction of colorless DTNB with GSH to generate yellow products (GSH depletion). (f) GSH-depleting capability of PEG-CS/PDA nanoparticles and Fe^{3+}@PEG-CS/PDA nanozymes under different condition (n = 3). (g) Schematic illustration of dual glutathione depletion and thermal/acidity-activated hydroxyl radical generation of Fe^{3+}@PEG-CS/PDA nanozymes.

using a NIB-100F inverted fluorescent biological microscope (Nanjing Jiangnan Novel Optics Co., Ltd., China) at excitation wavelengths of 488 nm for DCF.

2.12. In vitro cytotoxicity

4T1 cells (1×10^5 cells/well) seeded in a 6-well plate were incubated at 37 °C for 24 h in RPMI containing 10% FBS and 1% penicillin. The medium was then replaced with 1.0 mL of fresh medium containing PEG-CS/PDA nanoparticles or Fe^{3+}@PEG-CS/PDA nanozymes with different concentrations and the cells were further incubated at pH 7.4

and 6.5 for additional 24 h. Then, cells were washed twice with PBS and detached with trypsin-EDTA, followed by centrifugation (1500 rpm). The collected cell pellets dispersed in RPMI medium (150 μL) were irradiated by 808 nm NIR laser (1.25 W/cm²) for 5 min, followed by reseeding in a 12-well plate for additional 24-h incubation. MTT (0.25 mg/mL, 1.0 mL) was then added into each well, followed by incubation at 37 °C for 3 h. After discarding the culture medium, DMSO (0.8 mL) was added to dissolve the precipitate and the absorbance of the resulting solution at 570 nm was measured using a BioTek 800TS microplate reader. The viability of 4T1 cells treated with PEG-CS/PDA nanoparticles or Fe^{3+}@PEG-CS/PDA nanozymes without NIR laser
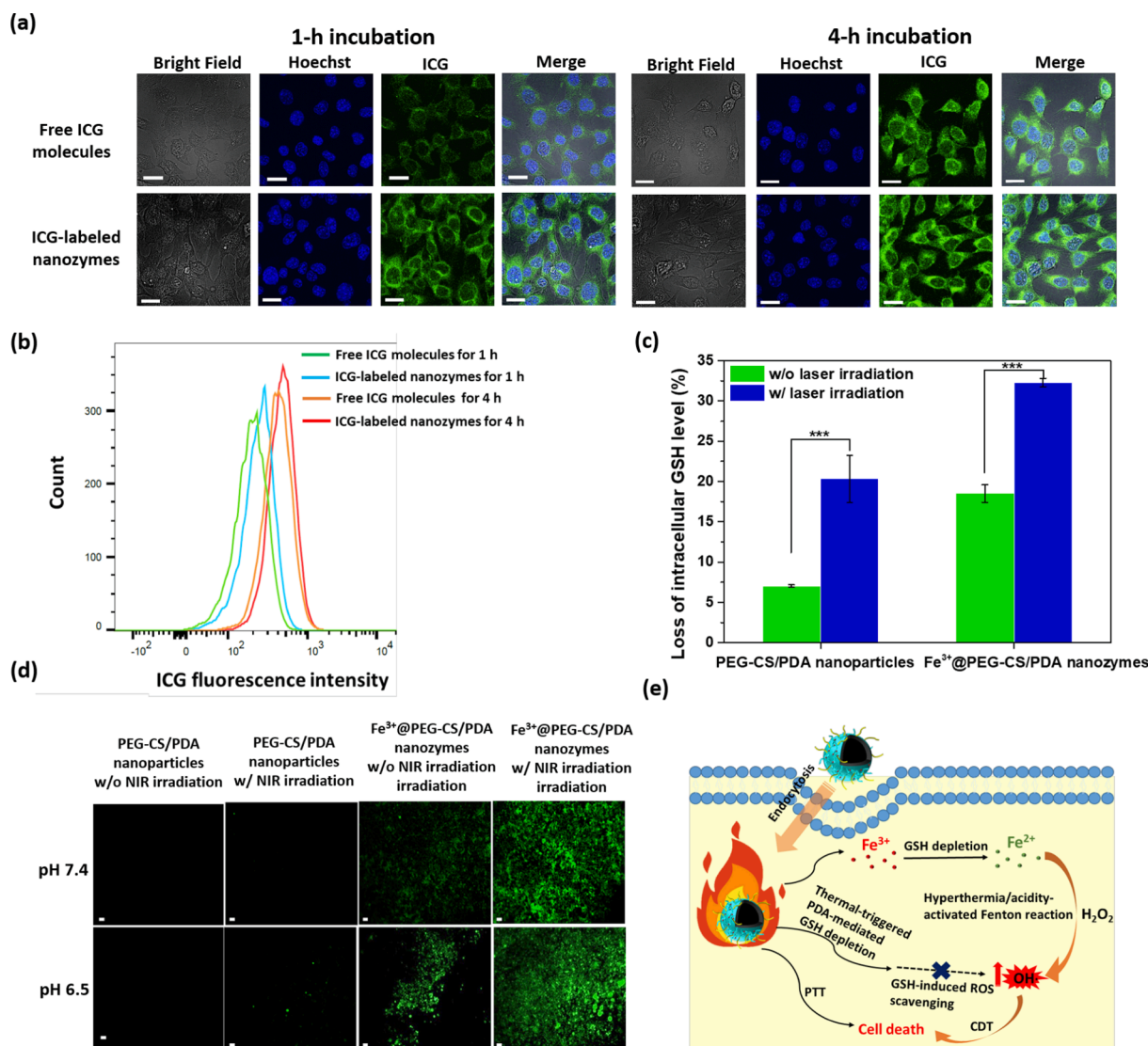
Fig. 5. (a) CLSM images of 4T1 cells incubated with ICG-labeled Fe^{3+}@PEG-CS/PDA nanozymes for 1 and 4 h, respectively, at 37 °C (ICG = 5 μM). Scale bars are 20 μm. (b) Flow cytometric histograms of 4T1 cells incubated with ICG-labeled Fe^{3+}@PEG-CS/PDA nanozymes for 1 and 4 h, respectively, at 37 °C (ICG = 5 μM). (c) Loss of intracellular GSH level of 4T1 cells treated with PEG-CS/PDA nanoparticles or Fe^{3+}@PEG-CS/PDA nanozymes with or without laser irradiation (n = 3). (d) DCF fluorescence of 4T1 cells incubated with either PEG-CS/PDA nanoparticles or Fe^{3+}@PEG-CS/PDA nanozymes with or without laser irradiation at pH 7.4 and 6.5. Scale bars are 100 μm. (e) Schematic illustration of the CDT/PTT combination therapy delivered by Fe^{3+}@PEG-CS/PDA nanozymes.

irradiation was also evaluated in a similar manner. On the other hand, the cytotoxicity of PEG-CS/PDA nanoparticles and Fe^{3+}@PEG-CS/PDA nanozymes against RAW 264.7 cells with or without laser irradiation was assessed by the same approach.

To explore the anticancer effect of the combined CDT and PTT, 4T1 cells (2×10^5 cells/well) were seeded in a 12-well plate were incubated with PEG-CS/PDA nanoparticles and Fe^{3+}@PEG-CS/PDA nanozymes (100 μg/mL), respectively, at pH 7.4 and 6.5 for 24 h. After that, cells were irradiated by 808 nm NIR laser (1.25 W/cm^2) for 5 min and gently washed with PBS twice to avoid washing off dead cells. The images of cells stained with calcein-AM (2 μM) and propidium iodide (PI, 4.5 μM) were attained using a NIB-100F inverted fluorescent biological microscope.

2.13. Animals and tumor model

Female BALB/c mice (5 ~ 6 weeks old) were purchased from National Laboratory Animal Center (Taiwan). The animal studies (IACUC Approval No: 2722) comply with the guidelines approved by the Administrative Committee on Animal Research in the Chung Shan Medical University (Taiwan). To establish the subcutaneous tumor model, 2×10^6 4T1 cells were subcutaneously injected into the right thigh of mice. Tumor volume (V) was calculated as follows: $V = L \times W^2/2$, where W is the tumor measurement at the widest point and L the tumor dimension at the longest point.

2.14. In vivo biodistribution and NIR-triggered tumor hyperthermia

After tumor volume had increased to 90 ~ 110 mm^3, PBS, free ICG molecules or ICG-labeled Fe^{3+}@PEG-CS/PDA nanozymes were injected into the mice via tail vein at an ICG dosage of 1.0 mg/kg. At 24 h post-injection, mice were sacrificed and the tumor and major organs were harvested. *Ex vivo* imaging was conducted using the IVIS (IVIS Lumina II, Caliper, LifeSciences, MA, USA) to evaluate the biodistribution of free ICG molecules and ICG-labeled nanozymes. To evaluate in vivo photo-triggered tumor hyperthermia, at 6 h post-injection, the tumor site of mice treated with PBS, PEG-CS/PDA nanoparticles or Fe^{3+}@PEG-CS/PDA nanozymes was irradiated with 808 nm laser (1.25 W/cm^2) for 5
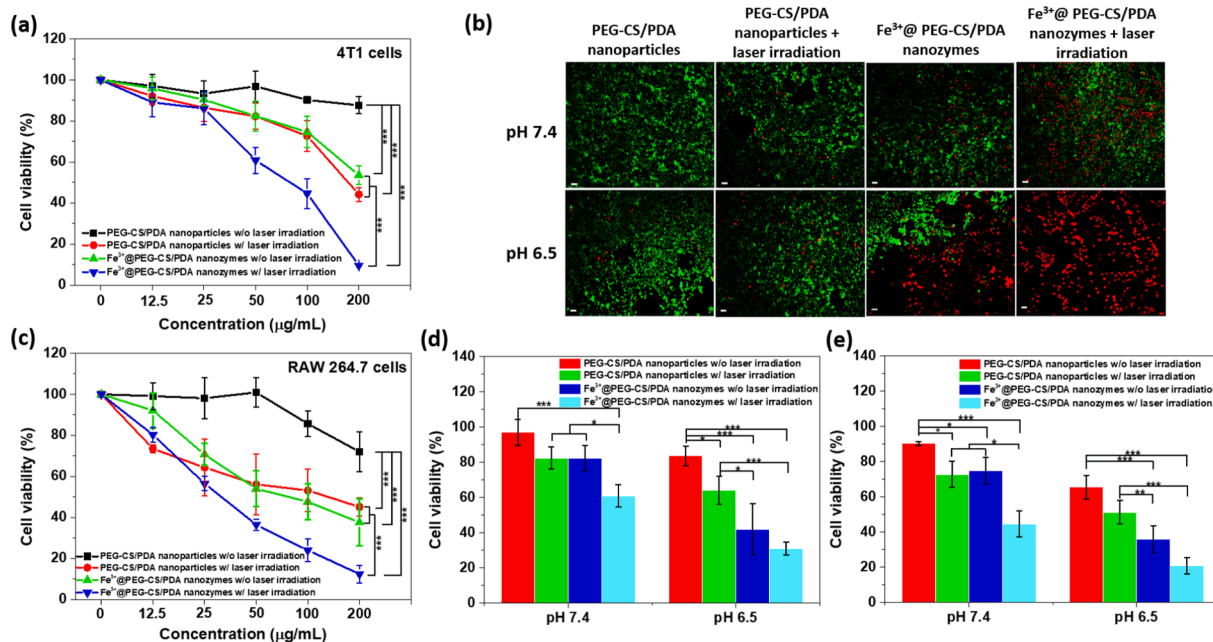
Fig. 6. (a) Cell viability of 4T1 cells incubated with different formulations at pH 7.4 for 24 h with or without the 5-min NIR laser irradiation, followed by additional 24 h incubation (n = 3). (b) Fluorescence images of 4T1 cells treated with either PEG-CS/PDA nanoparticles or Fe^{3+}@PEG-CS/PDA nanozymes (100 μg/mL) at pH 7.4 and 6.5 for 24 h with or without the 5-min NIR laser irradiation. The viable cells were stained green with calcein-AM, and the dead cells were stained red with PI. Scale bars are 100 μm. (c) Cell viability of RAW 264.7 cells incubated with different formulations at pH 7.4 for 24 h with or without the 5-min NIR laser irradiation, followed by additional 24 h incubation (n = 3). Cell viability of 4T1 cells incubated with different formulations of (d) 50 μg/mL and (e) 100 μg/mL at pH 7.4 and 6.5, respectively, for 24 h with or without the 5-min NIR laser irradiation, followed by additional 24 h incubation (n = 3). *p < 0.05, **p < 0.01, ***p < 0.001.

min. The tumor local temperature was monitored using an infrared thermal imaging camera.

2.15. In vivo tumor growth inhibition

When tumor volume of mice reached 90 ~ 110 mm³, mice were randomly divided into four groups (n = 5): (i) control; (ii) Fe^{3+}@PEG-CS/PDA nanozymes; (iii) PEG-CS/PDA nanoparticles + NIR laser; (iv) Fe^{3+}@PEG-CS/PDA nanozymes + NIR laser. Mice in different groups were intravenously injected with the corresponding reagents: (i) PBS (150 μL); (ii) Fe^{3+}@PEG-CS/PDA nanozymes (2 mg/mL, 150 μL); (iii) PEG-CS/PDA nanoparticles (2 mg/mL, 150 μL); (iv) Fe^{3+}@PEG-CS/PDA nanozymes (2 mg/mL, 150 μL). Each group was treated with a total of two doses at days 0 and 2. At 6 h post-injection, the tumor site of mice in corresponding groups were irradiated with 808 nm laser (1.25 W/cm²) for 5 min. The tumor volumes and body weight of different groups were measured every two days. At the 14th day, all mice were euthanized. The tumors and main organs (heart, liver, spleen, lung, kidney) were harvested and the tumor and spleen were weighted. The therapeutic index (TI) of different treatments was calculated by the following equation: TI (%) = $(1 - \frac{Weight\ of\ tumor\ in\ the\ experimental\ group}{Weight\ of\ tumor\ in\ the\ control\ group})$. The excised lung tissues were stained with Bouin's solution and the number of lung metastases was recorded. The excised tumors and organs were fixed with 4% paraformaldehyde and then processed routinely in paraffin. Next, the tumors and organs were sectioned to 4 μm thick slices for hematoxylin and eosin (H&E) staining and then observed by an Olympus IX70 inverted microscope (Japan). Furthermore, the tumor sections were stained with anti-Ki67 antibodies and then observed by digital microscope.

2.16. Statistical analysis

Data are reported as mean ± SD. The differences among groups were determined using one-way or two-way ANOVA analysis if statistically significant then post-hoc testing was performed with correction for

multiple comparisons; ns > 0.05, *p < 0.05, **p < 0.01, ***p < 0.001.

3. Results and discussion

3.1. Synthesis and characterization of PEG-CS conjugates

The mPEG-COOH used in the preparation of PEG-CS conjugates was attained by the ring-opening reaction of succinic anhydride with the terminated hydroxyl group of mPEG segments [43], and characterized by FT-IR and ¹H NMR spectroscopy (Fig. S2 and S3). The FT-IR spectrum of mPEG-COOH (Fig. S2) revealed the characteristic absorption bands of C—O and C—H stretching vibration at 1112 and 2887 cm⁻¹, respectively, and of C=O stretching vibration of carboxylic acid groups at 1735 cm⁻¹, indicating the successful conversion of hydroxyl end of mPEG segments into carboxylic acid group. Also, based on the signal integral ratio of the ethylene protons of succinic anhydride at δ 2.5 ppm and the methoxy protons of mPEG at δ 3.4 ppm as presented in the ¹H NMR spectrum of mPEG-COOH (Fig. S3a), the conjugation efficiency was calculated to be ca 95 %. Next, the PEG-CS conjugates were synthesized by the grafting reaction of mPEG-COOH with chitosan oligosaccharide in EDC/NHS-mediated manner. The characteristic bands of mPEG and chitosan segments were observed in the FT-IR spectrum of PEG-CS conjugates (Fig. S2). As shown in the ¹H NMR spectrum of PEG-CS conjugates (Fig. S3), the feature proton signals of mPEG-COOH at δ 3.7 and 3.4 ppm, respectively, and of chitosan at δ 3.0 and 2.0 ppm, respectively, were attained. These findings strongly confirm the successful conjugation of chitosan oligosaccharide with mPEG-COOH. The DS of chitosan with mPEG-COOH defined as the number of mPEG segments per 100 glucosamine units was obtained to be ca 8.44 according to the signal integral ratio of the methoxy protons of mPEG-COOH at δ 3.4 ppm and the glucosamine residue protons of chitosan at δ 3.0 ppm. Furthermore, in order to explore the effects of the surface decoration of PEG-CS conjugates with different DS values on the physicochemical properties of PEG-CS/PDA nanoparticles, the PEG-CS conjugates with various DS values were synthesized in a similar manner and
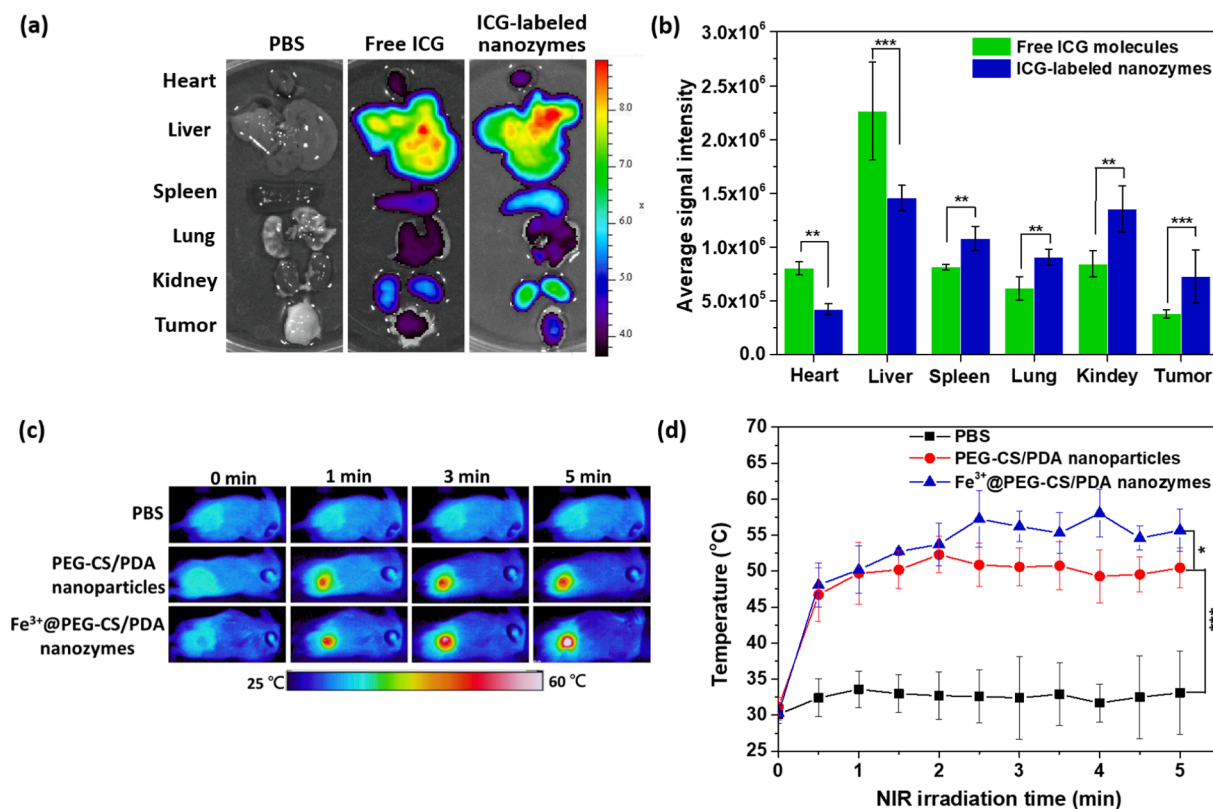
Fig. 7. (a) NIR fluorescence images and (b) average ICG fluorescence intensities of the isolated major organs and tumor at 24 h post-injection with different ICG-containing formulations (n = 3). (c) Infrared thermographic maps and (d) temperature profiles at the tumor sites of 4T1 tumor-bearing mice treated with PBS, Fe^{3+}@PEG-CS/PDA nanozymes or PEG-CS/PDA nanoparticles and irradiated with 808 nm NIR laser (1.25 W/cm^2) for 5 min at 6 h post-injection (n = 3). *p < 0.05, **p < 0.01, ***p < 0.001.

characterized by ^1H NMR measurement (Fig. S4).

3.2. Preparation and characterization of PEG-CS/PDA nanoparticles

As illustrated in Scheme 1a, PDA nanoparticles were first prepared by self-polymerization of DA molecules in NaOH solution at 50 °C. Notably, in the UV/Vis spectra (Fig. 1a), different from the appearing of only sharp absorption peak (281 nm) of DA monomers in aqueous solution, the considerably increased absorption from visible light to NIR light was observed for PDA nanoparticles due to the presence of various functional groups such as amine, carbonyl, and hydroxyl groups on the surface. Similar UV/Vis spectra of PDA nanoparticles were also attained in other studies [12,45]. The FT-IR spectrum of PDA nanoparticles showed two weak typical absorption bands of indole and indoline structure at 1607 and 1508 cm^{-1}, respectively (Fig. S2d). These results indicate the successful oxidative polymerization of DA molecules into PDA nanoparticles. The mean hydrodynamic diameter (D_h) and poly-dispersity index (PDI) of PDA nanoparticles in pH 7.4 0.01 M phosphate buffer were determined by DLS to be ca 129.1 ± 6.6 nm and 0.14 ± 0.02, respectively (Fig. S5 and S6). Note that after being dispersed into pH 7.4 0.15 M PBS for 6 h, the PDA nanoparticles exhibited remarkably enlarged particle size from 129.6 to beyond 800 nm (Fig. S6), being indicative of occurrence of inter-particle aggregation. Several studies also reported that the PDA nanoparticles in aqueous solution of salt concentration over 10 mM were apt to aggregate into large particles [46,47]. Such a poor colloidal stability of PDA nanoparticles in the milieu of physiological salt concentration largely limited their clinical application in tumor-targeted drug delivery. In order to improve the colloidal stability of PDA nanoparticles, through Michael reaction between primary amine residues of PEG-CS conjugates (DS: 8.44) and DHI units of PDA nanoparticles at a PEG-CS/PDA weight ratio of 1.5 in feed

(Scheme 1a), the hydrophilic PEG-CS conjugates were covalently attached on the surfaces of PDA nanoparticles. As shown in the XPS spectra (Fig. 1b, c and d), in addition to the feature peaks of pyridinc N (397.8 eV), pyrrolic N (399.6 eV) and graphitic N (402.1 eV) from PDA nanoparticles, the new peaks of amine (399.4 eV) and amide (399.7 eV) from PEG-CS conjugates were observed for hybrid PEG-CS/PDA nanoparticles. Also, compared to the PDA nanoparticles, the PEG-CS/PDA nanoparticles showed the appreciably lowered intensity of feature peak of C═C (283.9 eV) and enhanced intensity of characteristic peak of C—N (286.5 eV) (Fig. S7). The results confirm the successful coupling of PEG-CS adducts with PDA nanoparticles. Next, the weight ratio of PEG-CS and PDA within the hybrid nanoparticles was determined by TGA. The TGA profiles further illustrated that the hybrid PEG-CS/PDA nanoparticles were composed of ca 55 wt% PEG-CS and 45 wt% PDA (Fig. 1f).

Notably, the zeta potential of PEG-CS/PDA nanoparticles in aqueous solution of pH 7.4 was ca −6.0 mV, being significantly lower than that (ca −31.8 mV) of PDA nanoparticles (Fig. 2a). Such a reduced zeta potential of PEG-CS/PDA nanoparticles could be attributed to the charge neutralization between positively-charged PEG-CS conjugates and negative-charged PDA nanoparticles. Also, the outer PEG-CS-constituted layer of PEG-CS/PDA nanoparticles possibly partly shield the negatively-charged phenolic hydroxyl groups of PDA core. In addition, with the medium pH being adjusted from pH 7.4 to 5.0, the promoted protonation of chitosan segments on the surfaces of PEG-CS/PDA nanoparticles led to the conversion in zeta potentials of hybrid nanoparticles from negative to slightly positive values. As revealed in the angle-dependent DLS/SLS data of PEG-CS/PDA nanoparticles (Fig. 2b), a high linear correlation between the Γ and q^2, and the R_g/R_h ratio of ca 0.79 similar to that (0.78) of uniform rigid nanoparticles were attained. This indicates that the PEG-CS/PDA nanoparticles have a spherical
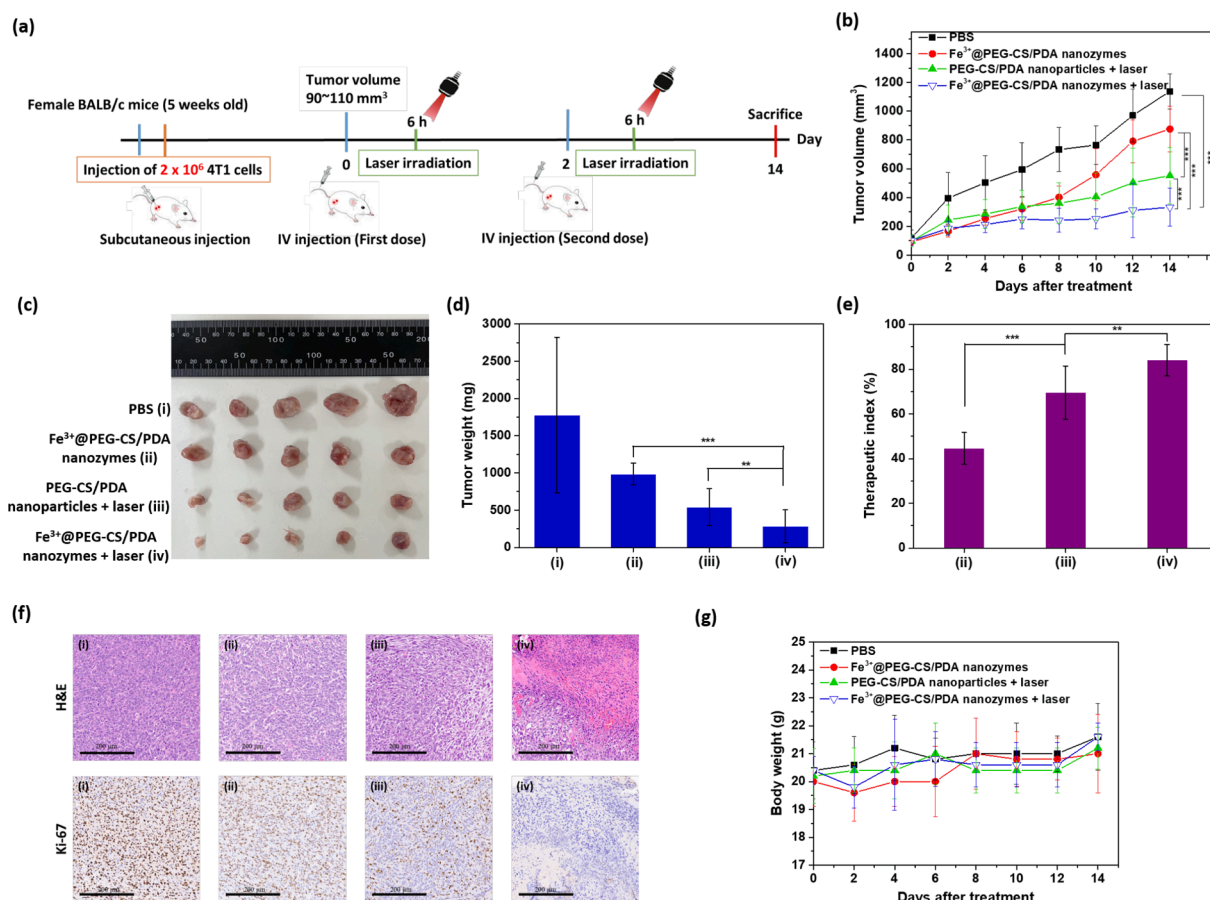
Fig. 8. (a) Experimental flowchart of in vivo tumor growth inhibition study. (b) Tumor growth inhibition profiles of 4T1 tumor-bearing mice injected Fe^{3+}@PEG-CS/PDA nanozymes or PEG-CS/PDA nanoparticles, followed by NIR laser irradiation (5 min, 1.25 W/cm^2) at 24 h post-injection or without any laser irradiation (n = 5). (c) Photographs and (d) weight of the tumors harvested from the euthanized mice at day 14 after the treatment (n = 5). (e) Therapeutic index value of different treatments (n = 5). (f) H&E and Ki67 staining of tumor sections from 4T1 tumor-bearing mice treated with (i) PBS, (ii) Fe^{3+}@PEG-CS/PDA nanozymes without laser irradiation, (iii) PEG-CS/PDA nanoparticles and (iv) Fe^{3+}@PEG-CS/PDA nanozymes with laser irradiation. Scale bars are 200 μm. (g) Body weight of 4T1 tumor-bearing mice receiving different treatments with or without NIR laser irradiation (n = 5). *p < 0.05, **p < 0.01, ***p < 0.001.

shape composed of a solid PDA core covered by PEG-CS layer. The well-dispersed spherical morphology of PEG-CS/PDA nanoparticles was also observed by their TEM and SEM images (Fig. 2c). On the other hand, when the weight ratio of PEG-CS conjugates (DS: 8.44) and PDA nanoparticles in feed was increased from 0.25 to 1.5, the particle size of PEG-CS/PDA nanoparticles in pH 7.4 phosphate buffer (0.01 M) was slightly increased from 133.8 to 144.6 nm (Fig. S5), being ascribed to that the incorporation of more PEG-CS conjugates into PDA nanoparticles could enlarge thickness of PEG-CS coating layer. Importantly, after transferring the nanoparticle samples to pH 7.4 0.15 M PBS, different from the considerably enlarged particle size of PDA nanoparticles due to salt-induced inter-particle flocculation (Fig. S6), the variation in particle size of PEG-CS/PDA nanoparticles was remarkably reduced with the raised PEG-CS/PDA weight ratios in feed (Fig. 2d). Note that the PEG-CS/PDA nanoparticles (PEG-CS/PDA weight ratio = 1.5) dispersed in pH 7.4 0.01 M phosphate buffer and 0.15 M PBS, respectively, for 6 h exhibited nearly similar particle size (ca 144.6 nm) and size distribution (PDI 0.134) (Fig. S5 and S8). Also, a virtually unchanged particle size of PEG-CS/PDA nanoparticles in 10 % FBS-containing RPMI medium at 37 °C for 24 h was attainted (Fig. 2e). These results suggest that the sufficient number of PEG-CS conjugates coated on the surfaces of PDA nanoparticles could not only prevent the salt-elicited inter-particle aggregation but also promote colloidal stability of hybrid nanoparticles in the presence of serum protein. Furthermore, in order to explore the effect of PEG content on the colloidal stability of PEG-CS/PDA nanoparticles in 0.15 M PBS, at a fixed PEG-CS/PDA weight ratio of 1.5:1 in feed, the

PEG-CS conjugates of different DS values were utilized in the preparation of PEG-CS/PDA nanoparticles. As presented in Fig. 2f, the particle size of PEG-CS (DS: 5.65)/PDA nanoparticles in 0.15 M PBS was determined to be ca 354.9 nm, being appreciably larger than that (144.6 nm) of PEG-CS (DS:8.44)/PDA nanoparticles under the same condition. Also, when the PEG-CS (DS: 4.41)/PDA nanoparticles were dispersed in pH 7.4 0.15 M PBS, visible precipitates were observed (inset of Fig. 2f). As a result, it can be demonstrated that the adequate amount of PEG segments on the surfaces of PEG-CS/PDA nanoparticles plays a vital role in the colloidal dispersion. In view of the above findings, the PEG-CS/PDA nanoparticles fabricated from the coupling of PEG-CS conjugates (DS: 8.44) and PDA nanoparticles at a weight ratio of 1.5:1 showed prominent colloidal stability in the serum-containing solution of physiological salt concentration, thus being selected as carriers to achieve tumor-targeted Fe^{3+} delivery.

3.3. NIR-triggered photothermal activity of PEG-CS/PDA nanoparticles

Several studies pointed out that the PDA-containing nanoparticles efficiently converted NIR light into heat by non-radiative decay, thus being available in cancer PTT [39,40,47]. In order to assess the NIR-triggered photothermal effect of PEG-CS/PDA nanoparticles, the temperature changes of hybrid nanoparticle solutions exposed to NIR laser irradiation of 808 nm were monitored by an infrared thermal imaging camera. Under NIR laser irradiation (power density of 1.0 W/cm^2) for 300 s, the aqueous solutions containing either PDA nanoparticles or
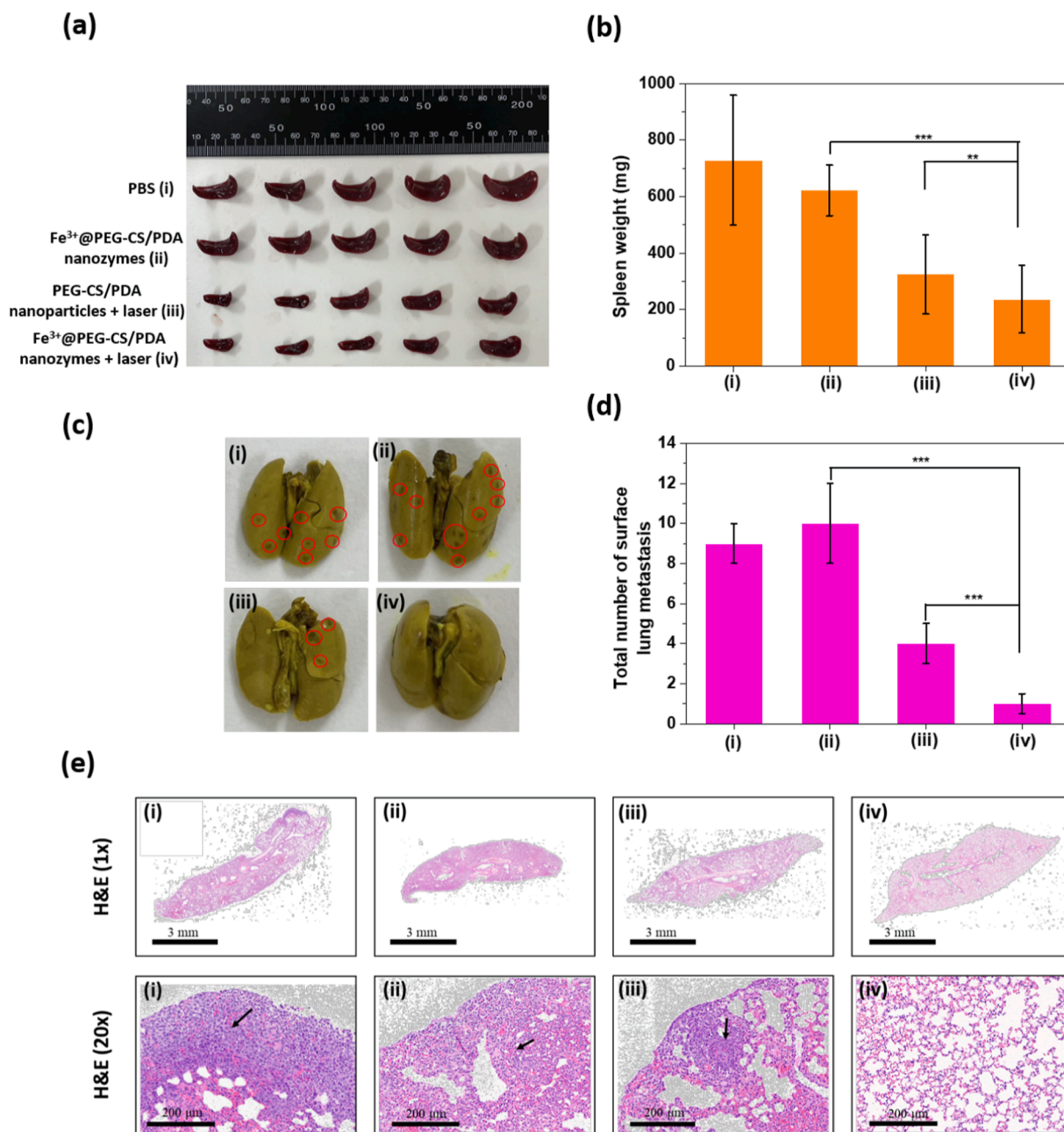
Fig. 9. (a) Photographs and (b) weight of the spleens harvested from the euthanized mice at day 14 after the treatment (n = 5). (c) Representative photographs and (d) average number of surface lung metastases of the whole lungs from 4T1 tumor-bearing mice treated with (i) PBS, (ii) Fe^{3+}@PEG-CS/PDA nanozymes without laser irradiation, (iii) PEG-CS/PDA nanoparticles and (iv) Fe^{3+}@PEG-CS/PDA nanozymes with laser irradiation (n = 3). The circled regions in the middle panels are the sites of tumor metastasis. (e) H&E staining of lung tissue sections from 4T1 tumor-bearing mice treated with (i) PBS, (ii) Fe^{3+}@PEG-CS/PDA nanozymes without laser irradiation, (iii) PEG-CS/PDA nanoparticles and (iv) Fe^{3+}@PEG-CS/PDA nanozymes with laser irradiation. The arrows are indicating tumor metastasis. $*p < 0.05$, $**p < 0.01$, $***p < 0.001$.

PEG-CS/PDA nanoparticles at the same PDA concentration (90 µg/mL) exhibited considerable temperature raise from 28 to ca 48 °C, being enough to evoke tumor ablation, whereas phosphate buffer maintained almost unaltered temperature (Fig. 3a and b). Based on the photo-thermal heating–cooling curves (Fig. 3c), the photothermal conversion efficiencies (η) of PEG-CS/PDA nanoparticles was determined to be ca 40.8 %, which is higher than that of the previously reported photo-thermal agents, such as gold nanorod and nanoshell (22 ∼ 30 %) [48,49], MoS_2 nanosheets (24.4 %) and copper sulfide nanoparticles (25.3 %) [50,51], and similar to that (40.7 %) of the pristine PDA nanoparticles (Fig. S9). The results indicate that the photothermal conversion capability of PEG-CS/PDA nanoparticles could not be affected by the PEG-CS coating layer and the PEG-CS/PDA nanoparticles show promising prospects for PTT application. Importantly, distinct from small organic photothermal agents with poor photostability, the PEG-CS/PDA nanoparticles receiving three cycles of continuous NIR laser irradiation still retained not only intact photothermal conversion ability (Fig. 3d), but also virtually unvaried particle size and zeta po-tential (Fig. 3e), signifying their prominent photothermal stability.

3.4. Preparation and characterization of Fe^{3+}@PEG-CS/PDA nanozymes

Considering that the Fe-based nanocatalysts have been extensively utilized in CDT by executing intratumoral Fenton or Fenton-like

reactions to elicit oxidative damage to tumor, to realize effective antitumor potency by the combination of PTT with CDT, the Fe^{3+}@PEG-CS/PDA nanozymes were prepared by chelation of ferric ions with the catechol groups of PDA cores using ferric chloride as the Fe^{3+} source. As shown in the XPS spectrum of Fe^{3+}@PEG-CS/PDA nanozymes (Fig. 1e), the appearing of the shakeup satellite peak at ca 711.0 eV (Fe $2p_{3/2}$) and central peak centered at 725.0 eV (Fe $2p_{1/2}$) indicates the existence of ferric cations. The ferric ion loading content of Fe^{3+}@PEG-CS/PDA nanozymes was determined by ICP-AES to be 7.94 ug/mg. After being chelated with ferric ions, the particle size of PEG-CS/PDA nanoparticle was somewhat enlarged from 144.6 to 151.6 nm. Furthermore, the Fe^{3+}@PEG-CS/PDA nanozymes still retained a spherical core–shell shape and well-dispersed uniform colloidal structure as evidenced by the angle-dependent DLS/SLS data (Fig. S10), TEM and SEM images (Fig. 2c). The energy dispersive EDS images showed that ferric ions were evenly distributed in the Fe^{3+}@PEG-CS/PDA nanozymes (Fig. 2c).

The Fe^{3+}@PEG-CS/PDA nanozymes dispersed in pH 7.4 0.15 M PBS or serum-containing RPMI medium maintained sound colloidal stability, being similar to PEG-CS/PDA nanoparticles (Fig. 2e and S11). Note that the Fe^{3+}@PEG-CS/PDA nanozymes became nearly neutral on their surfaces in response to pH reduction from 7.4 to 6.5 (close to acidic tumor microenvironment) due to the charge neutralization of protonated chitosan with negatively-charged PDA (Fig. 2a), but maintained virtually unchanged particle size in pH 6.5 FBS-containing RPMI medium for 24 h (Fig. S12a). Apparently, under serum-containing weak acidic condition, the outer hydrophilic PEG segments of the neutral nanozymes could effectively hinder the adsorption of serum protein, thereby preventing inter-nanozyme aggregation. This is beneficial for the infiltration of these nanozymes into deep tumor tissue in vivo. On the other hand, the Fe@PEG-CS/PDA nanozymes stored in pH 8.0 phosphate buffer at 4 °C for 28 days maintained nearly unchanged particle size (Fig. S12b), suggesting the sound colloidal stability of these nanozymes during storage period. Furthermore, after three on/off cycles of NIR laser irradiation, these nanozymes still retained virtually unvaried particle size, zeta potential and photo-elicited hyperthermia capability (Fig. 3e and 13a), indicating their robust photothermal stability. With the solution pH being adjusted from 7.4 to 5.0, the cumulative Fe^{3+} release of Fe@PEG-CS/PDA nanozymes over 12 h was increased from 10.2 to 43.7 % (Fig. 2g). Such an acidity-triggered Fe^{3+} release could be resulted from the declined coordination interaction between PDA and Fe^{3+} elicited by the promoted protonation of catechol groups under acidic condition. Similar observation was also obtained elsewhere [3,52]. The photothermal conversion efficiencies (η) of Fe^{3+}@PEG-CS/PDA nanozymes was determined to be ca 43.7 % (Fig. S13b), being somewhat higher than that (40.7 %) of PEG-CS/PDA nanoparticles. As expected, the photo-triggered temperature elevation of aqueous solutions containing Fe^{3+}@PEG-CS/PDA nanozymes was dependent on the nanozyme concentration and the power density of 808 nm NIR laser (Fig. 3f and S13c).

3.5. Cascade catalytic property of nanozymes

In spite of that the catalytic efficiency of Fe^{3+} is lower than that of Fe^{2+} in H_2O_2-involved Fenton reaction, some studies showed that Fe^{3+} could be reduced into Fe^{2+} by GSH, a main intracellular antioxidant [12,25], thus partly promoting intracellular ·OH production. To confirm if the Fe^{3+}@PEG-CS/PDA nanozymes could generate Fe^{2+} in the presence of GSH (10 mM), the Phe assay was used. As shown in Fig. 4a, the remarkable increase of absorbance within 400 ~ 525 nm was attained for the Fe^{3+}@PEG-CS/PDA nanozymes in the presence of GSH, whereas no significant variation in absorbance of the same wavelength range was observed for the Fe^{3+}@PEG-CS/PDA nanozymes in the lack of GSH and PEG-CS/PDA nanoparticles in the existence of GSH. Also, after addition of GSH, the Fe^{3+}@PEG-CS/PDA nanozyme solution was appreciably changed from brown to red-brown (inset of Fig. 4a). The results suggest that Fe^{2+} could be produced from the GSH-mediated reduction of Fe^{3+}

released from Fe^{3+}@PEG-CS/PDA nanozymes, thereby forming tangerine complex with Phe [25]. Next, we investigated the ·OH-generating activity of Fe^{3+}@PEG-CS/PDA nanozymes in the presence of H_2O_2 using MB as a probe of ·OH generation. As presented in Fig. 4b, the normalized absorbance of MB in Fe^{3+}@PEG-CS/PDA nanozyme solution (pH 7.4) containing 10 mM GSH for 2 h was somewhat decreased compared to that of MB in the counterparts in the absence of GSH. This indicates that the Fe^{2+} from reduction of Fe^{3+} by GSH could promote conversion of H_2O_2 into ·OH upon Fenton reaction, thus accelerating MB degradation. Importantly, as the pH of Fe^{3+}@PEG-CS/PDA nanozyme solution was changed from 7.4 to 5.5, in the existence of GSH, the normalized absorbance of MB was further declined (Fig. 4b). The catalytical property of Fe^{3+}@PEG-CS/PDA nanozymes was also validated by ABTS assay (Fig. 4c). In the presence of 8 mM H_2O_2, the increased absorption from visible light to NIR light and the formation of green oxidized ABTS were observed in aqueous solutions of Fe^{3+}@PEG-CS/PDA nanozymes in response to pH change from 7.4 to 5.5, in particularly for the GSH-containing sample solution. These findings suggest that the Fe^{2+} ions from GSH-treated Fe^{3+}@PEG-CS/PDA nanozymes could markedly promote Fenton reaction efficiency under weak acidic condition, thereby enhancing decomposition of H_2O_2 into ·OH to oxidize MB and ABTS. These results were also well consistent with those of other previous studies [18,25]. Furthermore, to imitate the photothermal-enhanced Fenton reaction, in the presence of GSH, the absorbance of MB in Fe^{3+}@PEG-CS/PDA nanozyme solution (pH 5.5) at 25, 37 and 50 °C, respectively, for 2 h was measured. Obviously, the MB absorbance was further decreased in response to solution temperature raise from 25 to 50 °C (Fig. 4d), suggesting that the temperature elevation could accelerate nanozyme-mediated Fenton reaction to promote MB degradation.

On the other hand, we explored the GSH depletion ability of Fe^{3+}@PEG-CS/PDA nanozymes by the Ellman assay [12], where colorless DTNB was reduced by GSH to form yellow products with a representative absorption peak at 412 nm. As presented in Fig. 4e and f, the absorbance of the reduced DTNB in aqueous solutions of GSH pretreated with PEG-CS/PDA nanoparticles was considerably diminished in response to temperature elevation from 25 to 50 °C, indicating that the quinone-rich PEG-CS/PDA nanoparticles efficiently consumed GSH with the increased temperature by irreversibly reacting with thiol groups of GSH by Michael addition reaction. Similar thermal-activated GSH depletion ability of PDA-based nanoparticles was also reported elsewhere [12]. Notably, the Fe^{3+}@PEG-CS/PDA nanozymes at 37 and 50 °C, respectively, showed capability of consuming GSH superior to PEG-CS/PDA nanoparticles. Based on the obtained results (Fig. 4a, e and f), it was verified that the Fe^{3+}@PEG-CS/PDA nanozymes potently consumed GSH by the PDA-mediated thiol-quinone reaction combined with Fe^{2+}/Fe^{3+} redox couples (Fig. 4g). Encouraged by the above findings, the nanozymes are anticipated to realize anticancer efficacy of photothermal-augmented CDT by the thermal/acidity-activated ·OH generation and sufficient GSH depletion capable of arresting ROS scavenging.

3.6. In vitro cellular uptake, intracellular GSH depletion and ROS generation

To assess the cellular internalization of Fe^{3+}@PEG-CS/PDA nanozymes by fluorescence imaging, the amphiphilic fluorescent dye, ICG, was incorporated into these nanozymes. As revealed in Fig. S14, compared to free ICG, the ICG-labeled Fe^{3+}@PEG-CS/PDA nanozymes exhibited remarkable red shift of characteristic ICG absorption peak from 790 to beyond 850 nm, being indicative of successful attachment of ICG molecules to the PDA cores upon the hydrophobic and π-π stacking interaction. Similar results were also reported elsewhere [53,54]. Notably, with 1-h incubation at 37 °C, the cytoplasm of 4T1 cells treated with ICG-labeled nanozymes exhibited appreciable ICG fluorescence compared to that of cells incubated with free ICG molecules (Fig. 5a).

This signifies that the uptake of ICG-carrying nanozymes by 4T1 cells could be efficiently promoted upon endocytosis, whereas the cellular internalization of free ICG molecules was hindered due to their negatively-charged sulfonate groups. With the incubation time being prolonged from 1 to 4 h, the cellular internalization of ICG-labeled nanozymes by 4T1 cells was further increased as reflected by the enhanced ICG fluorescence signal in the cytoplasm. Similar findings were also confirmed by flow cytometric histograms (Fig. 5b). Next, the GSH depletion capability of Fe^{3+}@PEG-CS/PDA nanozymes within 4T1 cells was evaluated by DTNB assay. As presented in Fig. 5c, in the absence of 808 nm NIR laser irradiation, the PEG-CS/PDA nanoparticles slightly reduced intracellular GSH level by ca 7 %, confirming the PDA-mediated GSH depletion upon Michael reaction as observed previously. By contrast, the intracellular GSH level of 4T1 cells incubated with Fe^{3+}@PEG-CS/PDA nanozymes was appreciably reduced by 18.5 %, demonstrating that the endocytosed nanozymes conducted dual GSH consumption by GSH-mediated reduction of Fe^{3+} ions combined with PDA-involved Michael reaction. Notably, with NIR laser irradiation, the Fe^{3+}@PEG-CS/PDA nanozymes and PEG-CS/PDA nanoparticles further declined intracellular GSH level by 32.3 and 20.4 %, respectively. This result illustrates that the NIR-triggered intracellular hyperthermia could accelerate Michael reaction of intracellular GSH and PDA component, thus considerably promoting GSH depletion, which coincides with the results as revealed in Fig. 4f.

On the other hand, to explore intracellular ROS generation of Fe^{3+}@PEG-CS/PDA nanozymes, the intracellular ROS levels were detected with DCFH-DA fluorogenic probe. As presented in Fig. 5d, no significant DCF fluorescence was observed in 4T1 cells exposed to PEG-CS/PDA nanoparticles at pH 7.4 or 6.5 with or without NIR laser irradiation, while the appreciable DCF fluorescence was attained in the Fe^{3+}@PEG-CS/PDA nanozyme group. This suggests that the Fe^{3+}@PEG-CS/PDA nanozymes endocytosed by 4T1 cells could facilitate intracellular ·OH generation via Fenton reaction between Fe^{3+}/Fe^{2+} and endogenous H_2O_2. More importantly, with 808 nm NIR laser irradiation, the DCF fluorescence signals of 4T1 cells incubated with Fe^{3+}@PEG-CS/PDA nanozymes at pH 7.4 or 6.5 were considerably boosted. The above findings strongly verifies that the endocytosed nanozymes efficiently promoted intracellular GSH depletion and ·OH production via photo-triggered hyperthermia, thus remarkably enhancing ROS accumulation (Fig. 5e). Moreover, several studies disclosed that the intracellular ·OH generation was increased by the photothermal-enhanced Fenton reaction [9,23,55,56].

3.7. In vitro anticancer potency of nanozymes

Encouraged by the outstanding photothermal effect, hyperthermia-activated ·OH generation and GSH depletion performance of Fe^{3+}@PEG-CS/PDA nanozymes, their anticancer capability on 4T1 cells was further investigated. As an important control, 4T1 cells incubated with PEG-CS/PDA nanoparticles in the concentration range 12.5–200 μg/mL at pH 7.4 for 24 h in the lack of NIR laser irradiation maintained high viability beyond 90 % (Fig. 6a), indicating minor toxicity of PEG-CS/PDA nanoparticles on cancer cells. By contrast, with 5-min NIR laser irradiation, the viability of 4T1 cells treated with PEG-CS/PDA nanoparticles was reduced to some extent in the nanoparticle concentration-dependent manner, signifying that the PTT delivered by PEG-CS/PDA nanoparticles moderately killed cancer cells. Furthermore, in the lack of NIR laser irradiation, somewhat declined viability of 4T1 cells incubated with Fe^{3+}@PEG-CS/PDA nanozymes at pH 7.4 was attained, demonstrating the CDT-based anticancer effect of nanozymes. Notably, the viability of 4T1 cells receiving Fe^{3+}@PEG-CS/PDA nanozymes plus NIR laser irradiation was largely lowered. Also, the IC_{50} value (the 50 % inhibitory concentration) of Fe^{3+}@PEG-CS/PDA nanozymes at pH 7.4 was markedly decreased from 243 to 72 μg/mL by NIR laser irradiation. With laser irradiation, the IC_{50} value (72 μg/mL) of Fe^{3+}@PEG-CS/PDA nanozymes is appreciably 2.6-fold lower that (186

μg/mL) of PEG-CS/PDA nanoparticles at pH 7.4 (Table S1). As revealed in the fluorescence staining of live/dead 4T1 cells (Fig. 6b), most of 4T1 cells treated with Fe^{3+}@PEG-CS/PDA nanozymes (100 μg/mL) at pH 7.4 combined with 5-min NIR laser irradiation showed remarkably stronger PI signals as compared to cells incubated with either the counterparts without NIR laser irradiation or PEG-CS/PDA nanoparticles with 5-min NIR laser irradiation. The data strongly demonstrated that the combination of CDT and PTT delivered by Fe^{3+}@PEG-CS/PDA nanozymes showed the highest efficacy in killing 4T1 cells, mainly due to the photothermal-enhanced intracellular ·OH generation combined with the NIR-triggered cellular heat injury, whereas the single nanozymes-based CDT or PEG-CS/PDA nanoparticles-mediated PTT only displayed limited anticancer effect. On the other hand, in the absence of NIR laser irradiation, the Fe^{3+}@PEG-CS/PDA nanozymes (12.5 ~ 200 μg/mL) showed few cytotoxicity on the healthy WS1 cells, human skin fibroblast cells, as reflected by relatively high viability of WS1 cells (beyond 90 %) (Fig. S15). Based on the results (Fig. 6a and S15), it could be proved the CDT delivered by Fe^{3+}@PEG-CS/PDA nanozymes selectively kills cancer cells rather than normal cells since H_2O_2 is overexpressed in cancer cells compared with normal cells, thus augmenting Fenton reaction-mediated ·OH generation within cancer cells [57].

Several studies report that the tumor-associated microphages (TAMs) have emerged as promising targets for cancer treatment due to the high correlation of TAMs to tumor progression and metastasis [58,59]. TAMs are also major innate immune cells that constitute up to 50% of the cell mass of human tumors. In order to further assess the feasibility of Fe^{3+}@PEG-CS/PDA nanozymes as an antitumor reagent, their cytotoxicity on the murine macrophages RAW 264.7 was evaluated. As presented in Fig. 6c, the viability of RAW 264.7 cells treated with Fe^{3+}@PEG-CS/PDA nanozymes plus NIR laser irradiation was remarkably reduced in comparison with that of cells receiving other treatments. Therefore, it can be demonstrated that the Fe^{3+}@PEG-CS/PDA nanozymes developed in this study could effectively kill 4T1 cells and macrophage-like RAW 264.7 cells upon the self-augmented CDT/PTT combination therapy. On the other hand, considering that the highly efficient Fenton catalytic reactions usually take place at a low pH environment [15,55,56] and the tumor microenvironment shows weak acidity (pH$_e$ 6.5 ~ 7.0), it was worthwhile to assess the cytotoxicity of Fe^{3+}@PEG-CS/PDA nanozymes on 4T1 cells under mimic tumor acidity condition. Notably, when the pH of culture medium was adjusted from 7.4 to 6.5, an appreciable decrease in cell viability of 4T1 cells treated with combined CDT and PTT delivered by Fe^{3+}@PEG-CS/PDA nanozymes (50 and 100 μg/mL) was obtained (Fig. 6d and e). Also, the CDT-mediated cytotoxicity of Fe^{3+}@PEG-CS/PDA nanozymes in response to the medium pH decrease from 7.4 to 6.5 was amplified. It should be noted that, when the milieu pH was changed from 7.4 to 6.5, the DCF and PI signals of 4T1 cells incubated with Fe^{3+}@PEG-CS/PDA nanozymes with or without laser irradiation were considerably enhanced as revealed in Fig. 5c and 6b. The above findings suggest that the Fe^{3+}@PEG-CS/PDA nanozymes effectively decompose intracellular H_2O_2 to generate ·OH by hyperthermia/acidity-enhanced Fenton catalytic efficiency, thus augmenting their cytotoxicity (Fig. 5e).

3.8. In vivo biodistribution and NIR-elicited tumor hyperthermia

To explore the in vivo biodistribution of Fe^{3+}@PEG-CS/PDA nanozymes by an IVIS imaging system, these nanozymes were labeled with amphiphilic ICG molecules. Free ICG molecules were adopted as the control group. At 6 h and 24 h post intravenous injection with free ICG molecules or ICG-labeled nanozymes, 4T1 tumor-bearing mice were sacrificed and the fluorescence images of major organ and tumor samples were attained. As presented in Fig. 7a, b and S16, compared to the tumor-bearing mice receiving free ICG molecules, the mice treated with ICG-labeled nanozymes showed appreciably higher ex vivo fluorescence signals of ICG in the tumor and kidney. Also, at 24 h post injection, the remarkably stronger ex vivo fluorescence intensity of livers of tumor-

bearing mice treated with free ICG molecules as compared to that of mice receiving ICG-labeled nanozymes was obtained. These findings indicate that these ICG-labeled nanozymes could be selectively accumulated at tumor site upon enhanced permeability and retention (EPR) effect and partly deposited within the kidney, whereas free ICG molecules show low tumor accumulation because the self-aggregation of massive ICG molecules during blood circulation causes their rapid uptake by the reticuloendothelial system of the liver [60,61]. Similar biodistributions of PDA-based nanoparticles in tumor-bearing mice have been observed in other studies [23,47].

The NIR-elicited in vivo tumor hyperthermia of tumor-bearing mice injected intravenously with Fe^{3+}@PEG-CS/PDA nanozymes or PEG-CS/PDA nanoparticles was observed by infrared thermal imaging. Under NIR laser irradiation of 808 nm at 6 h post intravenous injection, the tumor temperatures of Fe^{3+}@PEG-CS/PDA nanozymes-treated mice were slightly higher relative to that of PEG-CS/PDA nanoparticles-treated mice (Fig. 7c and d). This could be ascribed to that the Fe^{3+}@PEG-CS/PDA nanozymes exhibited a somewhat higher photothermal conversion efficiency than the PEG-CS/PDA nanoparticles (Fig. S13b and 3c). Importantly, after 5-min irradiation with the 808 nm NIR laser, tumor temperatures of the above two groups were beyond 50 °C. Such NIR-triggered tumor hyperthermia can cause irreversible heat damage against cancer cells.

3.9. Inhibition of in vivo tumor growth and metastasis by combination of CDT and PTT

Motivated by the excellent in vitro anticancer performance and satisfied in vivo tumor accumulation of Fe^{3+}@PEG-CS/PDA nanozymes, the in vivo antitumor effect was further studied using 4T1 tumor model in female BALB/c mice (Fig. 8a). As revealed in Fig. 8b, compared to PBS as the control group, the administration of Fe^{3+}@PEG-CS/PDA nanozymes without laser irradiation or PEG-CS/PDA nanoparticles with laser irradiation led to a considerable inhibition on tumor growth up to 8 days after treatment, beyond which the tumor of the treated mice progressively enlarged due to the proliferation of residual cancer cells surviving CDT or PTT alone. This clearly illustrates that the single CDT or PTT were incapable of suppressing tumor growth in an effective manner. Notably, for the group receiving Fe^{3+}@PEG-CS/PDA nanozymes with laser irradiation, the self-augmented CDT/PTT combination therapy prominently inhibited tumor growth during a 14-day evaluation period. Also, after 14-day treatment, nearly complete disappearing of tumor was observed in 4T1 tumor-bearing mice receiving the combination of CDT and PTT (Fig. S17). In agreement with the results of the in vivo tumor growth inhibition, the size and weight of tumors excised from the sacrificed mice treated with Fe^{3+}@PEG-CS/PDA nanozymes plus laser irradiation were the smallest among the tumors receiving other treatments (Fig. 8c and d). As presented in Fig. 8e, the average therapeutic index (ca 84.1 %) of the combined CDT and PTT delivered by Fe^{3+}@PEG-CS/PDA nanozymes was remarkably higher than that of single CDT provided by Fe^{3+}@PEG-CS/PDA nanozymes without laser irradiation (44.6 %) and that of single PTT from PEG-CS/PDA nanoparticles with laser irradiation (69.5 %). As presented in the H&E staining images of the tumor sections (Fig. 8f), most of the cancer cells within 4T1 tumor receiving PBS maintained their normal morphology, while the tumor cells treated with single CDT were slightly damaged. Notably, the tumors treated with the combined CDT and PTT transported by Fe^{3+}@PEG-CS/PDA nanozymes showed quite massive cell apoptosis and necrosis as compared to the tumors receiving single PTT provided by PEG-CS/PDA nanoparticles. Also, the staining of Ki67 (an indicator for active cell proliferation) indicated a dramatic reduction in cell proliferation in the Fe^{3+}@PEG-CS/PDA nanozymes + laser group (Fig. 8f). Based on the above findings, it is concluded that the NIR-triggered hyperthermia of Fe^{3+}@PEG-CS/PDA nanozymes not only leads to potent thermal ablation of tumor but also largely promotes intratumoral ·OH generation, thus showing the highest antitumor

potency. Furthermore, no significant variation in body weight of the treated mice over time in all groups was observed, suggesting that these formulations used in this study did not cause serious acute toxicity (Fig. 8g).

On the other hand, splenomegaly caused by the leukemoid reactions is known to be a vital clinical symptom in the late stages of breast cancer [62,63]. The photo images and weight of spleens collected from the sacrificed mice at day 14 after receiving various treatments were revealed in Fig. 9a and b. Note that the spleens of mice treated with Fe^{3+}@PEG-CS/PDA nanozymes combined with NIR irradiation were smallest in size and lowest in weight among those of mice receiving other treatments. This suggests that the combined CDT and PTT of Fe^{3+}@PEG-CS/PDA nanozymes could efficiently avoid splenomegaly of treated mice by inhibiting 4T1 tumor growth in an effective manner. Furthermore, in view of that the 4T1 tumor model used in the therapeutic study spontaneously forms lung metastasis [64,65], it is worthy to investigate the antimetastatic effect of the combination of CDT and PTT delivered by Fe^{3+}@PEG-CS/PDA nanozymes. In this end, the lung tissues were collected from each group of mice and then stained with Bouin's solution. As shown in Fig. 9c, d and S18, the administration of Fe^{3+}@PEG-CS/PDA nanozymes with laser irradiation resulted in a significantly decreased number of surface lung metastatic nodules compared with other treatment groups. This finding was also consistent with the H&E images of the lung tissue sections which also showed appreciably diminished metastasis in the lungs of tumor-bearing mice treated with Fe^{3+}@PEG-CS/PDA nanozymes with laser irradiation (Fig. 9e). As illustrated in Fig. S19, none of treatment groups showed acute adverse effects on the major organs of mice, similar to the PBS group. Importantly, no significant metastasis of cancer cells was observed in the major organs of 4T1 tumor-bearing mice treated with Fe^{3+}@PEG-CS/PDA nanozymes with NIR irradiation, whereas the remarkable metastasis of cancer cells into liver and spleen was attained in other treatment groups. According to the previous studies that the tumor metastasis could be potently arrested by elimination of TAMs [64,66], it can be reasonably presumed that the Fe^{3+}@PEG-CS/PDA nanozymes showed outstanding antimetastatic capability due to their powerful cytotoxicity on macrophages-like RAW 264.7 upon the combined CDT and PTT (Fig. 6c). All of these results adequately demonstrated that the Fe^{3+}@PEG-CS/PDA nanozymes developed in this work not only potently inhibited primary tumor growth but also effectively suppressed tumor metastasis by the CDT/PTT combination therapy.

On the other hand, Lu's group reported that PDT not only provided the source of active oxygen for the Fenton reaction, thus enhancing ferroptosis and inhibiting tumor growth, but also effectively induced immunogenic cell death (ICD) and stimulate immunity [67]. Based on the aforementioned study, we hypothesized that the CDT/PTT combination therapy delivered by Fe^{3+}@PEG-CS/PDA nanozymes possibly led to ICD to activate immunity, thereby impeding tumor metastasis. Although more evidences are required to support our hypothesis, this study still shows novel visions in design of therapeutic nanozymes with great clinical translational prospect for tumor treatment. It is worth mentioning that the Fe^{3+}@PEG-CS/PDA nanozymes developed in this work showed excellent antitumor effect by CDT/PTT combination therapy, being comparable to other therapeutic nanoparticles with PDT/CDT/PTT synergistic properties [68,69]. Furthermore, because the combination of PDT, CDT and PTT needs complicate design of functionalized nanoparticles and the anticancer effect of PDT in tumor hypoxic regions is largely limited, the development of easy-to-prepare Fe^{3+}@PEG-CS/PDA nanozymes capable of effectively conducting CDT/PTT combined therapy in tumor tissue without oxygen supplementation is essentially required.

4. Conclusion

In summary, we have successfully developed the Fe^{3+}@PEG-CS/PDA nanozymes by the coordination of Fe^{3+} ions with PEG-CS/PDA

nanoparticles. The Fe^{3+}@PEG-CS/PDA nanozymes exhibited a solid spherical shape and outstanding colloidal stability in serum-containing milieu. Also, the nanozymes showed not only prominent photothermal conversion efficiency and structural stability but also acidity-triggered Fe^{3+} release. Notably, the Fe^{3+}-chelated nanozymes effectively converted H_2O_2 into ·OH by GSH-consuming and hyperthermia/acidity-enhanced Fe^{2+}/Fe^{3+}-mediated Fenton catalytic reactions. Compared to the previously reported enzyme-like nanoparticles that only led to limited depletion of intracellular GSH upon single redox reaction between the Fenton metal ions and GSH molecules [70–72], the Fe^{3+}@PEG-CS/PDA nanozymes designed in this work largely depleted intracellular GSH by the PDA-mediated Michael reaction and Fe^{3+}/Fe^{2+} redox couples. The in vitro cellular uptake and cytotoxicity studies demonstrated that the endocytosed Fe^{3+}@PEG-CS/PDA nanozymes effectively enhanced intracellular GSH depletion and ·OH generation upon NIR-triggered hyperthermia, thereby potently killing 4T1 cells and RAW 264.7 cells by the combination of CDT and PTT. The prominent CDT/PTT combination therapy of Fe^{3+}@PEG-CS/PDA nanozymes after tumor accumulation considerably suppressed 4T1 breast tumor growth in vivo and metastasis of cancer cells to major organs. With the emergence of more multivalent metal ions with forceful Fenton catalytic activity, it is expected that the PEG-CS/PDA nanoparticles developed as chelator of Fe^{3+} ions in this study could be suggestive for future nano-catalytic medicine design.

CRediT authorship contribution statement

Tzu-Hao Wang: Conceptualization, Methodology, Investigation, Formal analysis. **Ming-Yen Shen:** Investigation, Validation, Resources. **Nien-Tzu Yeh:** Investigation, Resources. **Yu-Hsin Chen:** Methodology, Validation. **Tsai-Ching Hsu:** Resources, Investigation. **Hao-Yang Chin:** Methodology, Validation. **Yi-Ting Wu:** Methodology, Investigation. **Bor-Show Tzang:** Investigation, Resources, Funding acquisition, Supervision, Writing – review & editing. **Wen-Hsuan Chiang:** Conceptualization, Writing – original draft, Writing – review & editing, Supervision, Project administration, Funding acquisition.

Declaration of Competing Interest

The authors declare that they have no known competing financial interests or personal relationships that could have appeared to influence the work reported in this paper.

Data availability

Data will be made available on request.

Appendix A. Supplementary material

Supplementary data to this article can be found online at https://doi.org/10.1016/j.jcis.2023.07.134.

References

[1] C. Zhang, W. Bu, D. Ni, S. Zhang, Q. Li, Z. Yao, J. Zhang, H. Yao, Z. Wang, J. Shi, Synthesis of iron nanometallic glasses and their application in cancer therapy by a localized Fenton reaction, Angew. Chem. Int. Ed. 55 (2016) 2101–2106.

[2] P. Ma, H. Xiao, C. Yu, J. Liu, Z. Cheng, H. Song, X. Zhang, C. Li, J. Wang, Z. Gu, J. Lin, Enhanced cisplatin chemotherapy by iron oxide nanocarrier-mediated generation of highly toxic reactive oxygen species, Nano Lett. 17 (2017) 928–937.

[3] L. Chen, Z. Lin, L. Liu, X. Zhang, W. Shi, D. Ge, Y. Sun, Fe^{2+}/Fe^{3+} ions chelated with ultrasmall polydopamine nanoparticles induce ferroptosis for cancer therapy, ACS Biomater. Sci. Eng. 5 (2019) 4861–4869.

[4] Z. Tang, Y. Liu, M. He, W. Bu, Chemodynamic therapy: tumour microenvironment-mediated Fenton and Fenton-like reactions, Angew. Chem. Int. Ed. 58 (2019) 946–956.

[5] S. Koo, O.K. Park, J. Kim, S.I. Han, T.Y. Yoo, N. Lee, Y.G. Kim, H. Kim, C. Lim, J. S. Bae, J. Yoo, D. Kim, S.H. Choi, T. Hyeon, Enhanced chemodynamic therapy by Cu-Fe peroxide nanoparticles: tumor microenvironment-mediated synergistic fenton reaction, ACS Nano 16 (2022) 2535–2545.

[6] H. Ranji-Burachaloo, P.A. Gurr, D.E. Dunstan, G.G. Qiao, Cancer treatment through nanoparticle-facilitated Fenton reaction, ACS Nano 12 (2018) 11819–11837.

[7] Y. Lin, X. Chen, C. Yu, G. Xu, X. Nie, Y. Cheng, Y. Luan, Radiotherapy-mediated redox homeostasis-controllable nanomedicine for enhanced ferroptosis sensitivity in tumor therapy, Acta Biomater. 159 (2023) 300–311.

[8] M. Zhang, X. Qin, Z. Zhao, Q. Du, Q. Li, Y. Jiang, Y. Luan, A self-amplifying nanodrug to manipulate the Janus-faced nature of ferroptosis for tumor therapy, Nanoscale Horiz. 7 (2022) 198–210.

[9] L. Zhang, H. Forgham, A. Shen, R. Qiao, B. Guo, Recent advances in single Fe-based nanoagents for photothermal-chemodynamic cancer therapy, Biosensors 12 (2022) 86.

[10] Q. Tian, F. Xue, Y. Wang, Y. Cheng, L. An, S. Yang, X. Chen, G. Huang, Recent advances in enhanced chemodynamic therapy strategies, Nano Today 39 (2021), 101162.

[11] B. Niu, K. Liao, Y. Zhou, T. Wen, G. Quan, X. Pan, C. Wu, Application of glutathione depletion in cancer therapy: Enhanced ROS-based therapy, ferroptosis, and chemotherapy, Biomaterials 277 (2021), 121110.

[12] J. Xiao, L. Hai, Y. Li, H. Li, M. Gong, Z. Wang, Z. Tang, L. Deng, D. He, An ultrasmall Fe_3O_4-decorated polydopamine hybrid nanozyme enables continuous conversion of oxygen into toxic hydroxyl radical via GSH-depleted cascade redox reactions for intensive wound disinfection, Small 18 (2022) 2105465.

[13] N. Gong, X. Ma, X. Ye, Q. Zhou, X. Chen, X. Tan, S. Yao, S. Huo, T. Zhang, S. Chen, X. Teng, X. Hu, J. Yu, Y. Gan, H. Jiang, J. Li, X.-J. Liang, Carbon-dot-supported atomically dispersed gold as a mitochondrial oxidative stress amplifier for cancer treatment, Nat. Nanotechnol. 14 (2019) 379–387.

[14] P.H.G.M. Willems, R. Rossignol, C.E.J. Dieteren, M.P. Murphy, W.J.H. Koopman, Redox homeostasis and mitochondrial dynamics, Cell Metab. 22 (2015) 207–218.

[15] C. Fang, Z. Deng, G. Cao, Q. Chu, Y. Wu, X. Li, X. Peng, G. Han, Co-ferrocene MOF/glucose oxidase as cascade nanozyme for effective tumor therapy, Adv. Funct. Mater. 30 (2020) 1910085.

[16] J.-X. Fan, M.-Y. Peng, H. Wang, H.-R. Zheng, Z.-L. Liu, C.-X. Li, X.-N. Wang, X.-H. Liu, S.-X. Cheng, X.-Z. Zhang, Engineered bacterial bioreactor for tumor therapy via Fenton-like reaction with localized H_2O_2 generation, Adv. Mater. 31 (2019) 1808278.

[17] S. Wang, Z. Wang, G. Yu, Z. Zhou, O. Jacobson, Y. Liu, Y. Ma, F. Zhang, Z.-Y. Chen, X. Chen, Tumor-specific drug release and reactive oxygen species generation for cancer chemo/chemodynamic combination therapy, Adv. Sci. 6 (2019) 1801986.

[18] L.S. Lin, J. Song, L. Song, K. Ke, Y. Liu, Z. Zhou, Z. Shen, J. Li, Z. Yang, W. Tang, Simultaneous Fenton-like ion delivery and glutathione depletion by MnO_2-based nanoagent to enhance chemodynamic therapy, Angew. Chem. Int. Ed. 57 (2018) 4902–4906.

[19] F. Zhao, J. Yao, Y. Tong, D. Su, Q. Xu, Y. Ying, W. Li, J. Li, J. Zheng, L. Qiao, W. Cai, X. Mou, S. Che, J. Yu, Y. Hou, H_2O_2-replenishable and GSH-depletive ROS 'bomb' for self-enhanced chemodynamic therapy, Mater. Adv. 3 (2022) 1191–1199.

[20] L.H. Fu, Y. Wan, C. Qi, J. He, C. Li, C. Yang, H. Xu, J. Lin, P. Huang, Nanocatalytic theranostics with glutathione depletion and enhanced reactive oxygen species generation for efficient cancer therapy, Adv. Mater. 33 (2021) 2006892.

[21] Y. Sang, F. Cao, W. Li, L. Zhang, Y. You, Q. Deng, K. Dong, J. Ren, X. Qu, Bioinspired construction of a nanozyme-based H_2O_2 homeostasis disruptor for intensive chemodynamic therapy, J. Am. Chem. Soc. 142 (2020) 5177–5183.

[22] Y. Zhou, S. Fan, L. Feng, X. Huang, X. Chen, Manipulating intratumoral Fenton chemistry for enhanced chemodynamic and chemodynamic-synergized multimodal therapy, Adv. Mater. 33 (2021) 2104223.

[23] Y. Chen, T. Wu, P. Gao, N. Li, X. Wan, J. Wang, W. Pan, B. Tang, A Cu^{2+} doped mesoporous polydopamine Fenton nanoplatform for low-temperature photothermal therapy, Mater. Chem. Front. 5 (2021) 6546–6552.

[24] H. Zhang, R. Han, P. Song, X. Wei, Y. Hou, J. Yu, K. Tang, Hydrogen peroxide self-sufficient and glutathione-depleted nanoplatform for boosting chemodynamic therapy synergetic phototherapy, J. Colloid Interface Sci. 629 (2023) 103–113.

[25] F. Liu, L. Lin, Y. Zhang, Y. Wang, S. Sheng, C. Xu, H. Tian, X. Chen, A tumor-microenvironment-activated nanozyme-mediated theranostic nanoreactor for imaging-guided combined tumor therapy, Adv. Mater. 31 (2019) 1902885.

[26] H. Sun, Y. Zhang, S. Chen, R. Wang, Q. Chen, J. Li, Y. Luo, X. Wang, H. Chen, Photothermal Fenton nanocatalysts for synergetic cancer therapy in the second near-infrared window, ACS Appl. Mater. Interfaces 12 (2020) 30145–30154.

[27] H. Yu, M. Ma, K. Liang, J. Shen, Z. Lan, H. Chen, A self-assembled metal-polyphenolic nanomedicine for mild photothermal-potentiated chemodynamic therapy of tumors, Appl. Mater. Today 25 (2021), 101235.

[28] C. Liu, D. Wang, S. Zhang, Y. Cheng, F. Yang, Y. Xing, T. Xu, H. Dong, X. Zhang, Biodegradable biomimic copper/manganese silicate nanospheres for chemodynamic/photodynamic synergistic therapy with simultaneous glutathione depletion and hypoxia relief, ACS Nano 13 (2019) 4267–4277.

[29] Y. Huang, Y. Jiang, Z. Xiao, Y. Shen, L. Huang, X. Xu, G. Wei, C. Xu, C. Zhao, Three birds with one stone: a ferric pyrophosphate based nanoagent for synergetic NIR-

triggered photo/chemodynamic therapy with glutathione depletion, Chem. Eng. J. 380 (2020), 122369.

[30] Y. Zhang, O. Eltayeb, Y. Meng, G. Zhang, Y. Zhang, S. Shuang, C. Dong, Tumor microenvironment responsive mesoporous silica nanoparticles for dual delivery of doxorubicin and chemodynamic therapy (CDT) agent, New J. Chem. 44 (2020) 2578–2586.

[31] R. Zhang, T. Liu, W. Li, Z. Ma, P. Pei, W. Zhang, K. Yang, Y. Tao, Tumor microenvironment-responsive BSA nanocarriers for combined chemo/chemodynamic cancer therapy, J. Nanobiotechnol. 20 (2022) 223.

[32] L. Feng, R. Xie, C. Wang, S. Gai, F. He, D. Yang, P. Yang, J. Lin, Magnetic targeting, tumor microenvironment-responsive intelligent nanocatalysts for enhanced tumor ablation, ACS Nano. 12 (2018) 11000–11012.

[33] C. Li, Y. Wan, Y. Zhang, L.H. Fu, N.T. Blum, R. Cui, B. Wu, R. Zheng, J. Lin, Z. Li, P. Huang, In situ sprayed starvation/chemodynamic therapeutic gel for post-surgical treatment of IDH1 (R132H) glioma, Adv. Mater. 34 (2022) 2103980.

[34] T. Wang, X. Xu, K. Zhang, Nanotechnology-enabled chemodynamic therapy and immunotherapy, Curr. Cancer Drug Targets 21 (2021) 545–557.

[35] P. Liu, Y. Peng, J. Ding, W. Zhou, Fenton metal nanomedicines for imaging-guided combinatorial chemodynamic therapy against cancer, Asian J. Pharm. Sci. 17 (2022) 177–192.

[36] G. Liu, J. Zhu, H. Guo, A. Sun, P. Chen, L. Xi, W. Huang, X. Song, X. Dong, Mo₂C-derived polyoxometalate for NIR-II photoacoustic imaging-guided chemodynamic/photothermal synergistic therapy, Angew. Chem. Int. Ed. 58 (2019) 18641–18646.

[37] B. Zhou, C. Yin, Q. Feng, Y. Wu, X. Pan, C. Liu, J. Tian, S. Geng, K. Wang, J. Xing, Polypyrrole-based nanotheranostic agent for MRI guided photothermal-chemodynamic synergistic cancer therapy, Nanoscale 13 (2021) 19085–19097.

[38] Q. Wang, F. Li, H. Yang, Y. Wang, W. Ding, F. Dai, L. Wei, S. Cao, W. Song, Simultaneous self-supply of H2O2 and GSH-depleted intracellular oxidative stress for enhanced photodynamic/photothermal/chemodynamic therapy, Chem. Commun. 58 (2022) 8536–8539.

[39] W.X. Zhang, Y.N. Hao, Y.R. Gao, Y. Shu, J.H. Wang, Mutual benefit between Cu(II) and polydopamine for improving photothermal-chemodynamic therapy, ACS Appl. Mater. Interfaces. 13 (2021) 38127–38137.

[40] B. Chen, Y. Cao, H. Zhao, F. Long, X. Feng, J. Li, X. Pan, A novel Fe³⁺-stabilized magnetic polydopamine composite for enhanced selective adsorption and separation of methylene blue from complex wastewater, J. Hazard. Mater. 392 (2020), 122263.

[41] H. Hu, X. Liu, J. Hong, N. Ye, C. Xiao, J. Wang, Z. Li, D. Xu, Mesoporous polydopamine-based multifunctional nanoparticles for enhanced cancer phototherapy, J. Colloid Interface Sci. 612 (2022) 246–260.

[42] A. Tyo, S. Welch, M. Hennenfent, P. Kord Fooroshani, B.P. Lee, R. Rajachar, Development and characterization of an antimicrobial polydopamine coating for conservation of humpback whales, Front. Chem. 7 (2019) 618.

[43] S.J. Huang, T.H. Wang, Y.H. Chou, H.M. Wang, T.C. Hsu, J.L. Yow, B.S. Tzang, W.H. Chiang, Hybrid PEGylated chitosan/PLGA nanoparticles designed as pH-responsive vehicles to promote intracellular drug delivery and cancer chemotherapy, Int. J. Biol. Macromol. 210 (2022) 565–578.

[44] P. Zhang, X.u. Qinan, X. Li, Y. Wang, pH-Responsive polydopamine nanoparticles for photothermally promoted gene delivery, Mater. Sci. Eng. C 108 (2020), 110396.

[45] Y. Lia, W. Hong, H. Zhang, T.T. Zhang, Z. Chen, S. Yuan, P. Peng, M. Xiao, L. Xu, Photothermally triggered cytosolic drug delivery of glucose functionalized polydopamine nanoparticles in response to tumor microenvironment for the GLUT1-targeting chemo-phototherapy, J. Control. Release 317 (2020) 232–245.

[46] A. Jin, Y. Wang, K. Lin, L. Jiang, Nanoparticles modified by polydopamine: Working as "drug" carriers, Bioact. Mater. 5 (2020) 522–541.

[47] M.H. Hsieh, T.H. Wang, S.H. Hu, T.C. Hsu, J.L. Yow, B.S. Tzang, W.H. Chiang, Tumor site-specific PEG detachment and active tumor homing of therapeutic PEGylated chitosan/folate-decorated polydopamine nanoparticles to augment antitumor efficacy of photothermal/chemo combination therapy, Chem. Eng. J. 446 (2022), 137243.

[48] J. Zeng, D. Goldfeld, Y.N. Xia, A plasmon-assisted optofluidic (PAOF) system for measuring the photothermal conversion efficiencies of gold nanostructures and controlling an electrical switch, Angew. Chem. Int. Ed. 52 (2013) 4169–4173.

[49] J.R. Cole, N.A. Mirin, M.W. Knight, G.P. Goodrich, N.J. Halas, Photothermal efficiencies of nanoshells and nanorods for clinical therapeutic applications, J. Phys. Chem. C 113 (2009) 12090–12094.

[50] W. Yin, L. Yan, J. Yu, G. Tian, L. Zhou, X. Zheng, X. Zhang, Y. Yong, J. Li, Z. Gu, Y. Zhao, High-throughput synthesis of single-layer MoS2 nanosheets as a near-infrared photothermal-triggered drug delivery for effective cancer therapy, ACS Nano 8 (2014) 6922–6933.

[51] A.C. Poulose, S. Veeranarayanan, M.S. Mohamed, Y. Nagaoka, R.R. Aburto, T. Mitcham, P.M. Ajayan, R.R. Bouchard, Y. Sakamoto, Y. Yoshida, T. Maekawa, D. S. Kumar, Multi-stimuli responsive Cu2S nanocrystals as trimodal imaging and synergistic chemo-photothermal therapy agents, Nanoscale 7 (2015) 8378–8388.

[52] H. Geng, Q.Z. Zhong, J. Li, Z. Lin, J. Cui, F. Caruso, J. Hao, Metal ion-directed functional metal-phenolic materials, Chem. Rev. 122 (2022) 11432–11473.

[53] F. Xu, M. Liu, X. Li, Z. Xiong, X. Cao, X. Shi, R. Guo, Loading of indocyanine green within polydopamine-coated laponite nanodisks for targeted cancer photothermal and photodynamic therapy, Nanomaterials 8 (2018) 347.

[54] X. Liu, N. Xu, X. Pu, G. Yin, Synthesis of ICG/PDA nanoparticles and their photothermal-photodynamic synergistic antitumor effect, Mater. Sci. 11 (2021) 918–928.

[55] Z. Xiao, W. Zuo, L. Chen, L. Wu, N. Liu, J. Liu, Q. Jin, Y. Zhao, X. Zhu, H2O2 self-supplying and GSH-depleting nanoplatform for chemodynamic therapy synergetic photothermal/chemotherapy, ACS Appl. Mater. Interfaces 13 (2021) 43925–43936.

[56] C. Du, L. Zhou, J. Qian, M. He, Z.G. Zhang, C. Feng, Y. Zhang, R. Zhang, C.M. Dong, Ultrasmall zwitterionic polypeptide-coordinated nanohybrids for highly efficient cancer photothermal ferrotherapy, ACS Appl. Mater. Interfaces 13 (2021) 44002–44012.

[57] C. Cao, X. Wang, N. Yang, X. Song, X. Dong, Recent advances of cancer chemodynamic therapy based on Fenton/Fenton-like chemistry, Chem. Sci. 13 (2022) 863–889.

[58] J. Condeelis, J.W. Pollard, Macrophages: obligate partners for tumor cell migration, invasion, and metastasis, Cell 124 (2006) 263.

[59] J.W. Pollard, Tumour-educated macrophages promote tumour progression and metastasis, Nat. Rev. Cancer 4 (2004) 71–78.

[60] M. Zheng, P. Zhao, Z. Luo, P. Gong, C. Zheng, P. Zhang, C. Yue, D. Gao, Y. Ma, L. Cai, Robust ICG theranostic nanoparticles for folate targeted cancer imaging and highly effective photothermal therapy, ACS Appl. Mater. Interfaces 6 (2014) 6709–6716.

[61] Z. Wan, H. Mao, M. Guo, Y. Li, A. Zhu, H. Yang, H. He, J. Shen, L. Zhou, Z. Jiang, C. Ge, X. Chen, X. Yang, G. Liu, H. Chen, Highly efficient hierarchical micelles integrating photothermal therapy and singlet oxygen-synergized chemotherapy for cancer eradication, Theranostics 4 (2014) 399–411.

[62] N. Xu, A. Hu, X. Pu, J. Li, X. Wang, J. Wang, Z. Huang, X. Liao, G. Yin, Fe(III)-chelated polydopamine nanoparticles for synergistic tumor therapies of enhanced photothermal ablation and antitumor immune activation, ACS Appl. Mater. Interfaces 14 (2022) 15894–15910.

[63] M. Liu, X. Jin, X. He, L. Pan, X. Zhang, Y. Zhao, Macrophages support splenic erythropoiesis in 4T1 tumor-bearing mice, PLoS ONE 10 (2015) e0121921.

[64] N. Guo, Y. Zhou, T. Wang, M. Lin, J. Chen, Z. Zhang, X. Zhong, Y. Lu, Q. Yang, D. Xu, J. Gao, M. Han, Specifically eliminating tumor-associated Macrophages with an extra- and intracellular stepwise-responsive nanocarrier for inhibiting metastasis, ACS Appl. Mater. Interfaces 12 (2020) 57798–57809.

[65] Y. Wang, Y. Xie, J. Li, Z.H. Peng, Y. Sheinin, J. Zhou, D. Oupicky, Tumor-penetrating nanoparticles for enhanced anticancer activity of combined photodynamic and hypoxia-activated therapy, ACS Nano 11 (2017) 2227–2238.

[66] L.Q. Fu, W.L. Du, M.H. Cai, J.Y. Yao, Y.Y. Zhao, X.Z. Mou, The roles of tumor-associated macrophages in tumor angiogenesis and metastasis, Cell. Immunol. 353 (2020), 104119.

[67] L. Tan, X. Shen, Z. He, Y. Lu, The role of photodynamic therapy in triggering cell death and facilitating antitumor immunology, Front Oncol. 12 (2022), 863107.

[68] W. Liu, Q. Yan, C. Xia, X. Wang, A. Kumar, Y. Wang, Y. Liu, Y. Pane, J. Liu, Recent advances in cell membrane coated metal-organic frameworks (MOFs) for tumor therapy, J. Mater. Chem. B 9 (2021) 4459–4474.

[69] W. Chen, M. Liu, H. Yang, A. Nezamzadeh-Ejhieh, C. Lu, Y. Pan, J. Liu, Z. Bai, Recent advances of Fe(III)/Fe(II)-MPNs in biomedical applications, Pharmaceutics 15 (2023) 1323.

[70] J. Dong, Y. Yu, Y. Pei, Z. Pei, pH-Responsive aminotriazole doped metal organic frameworks nanoplatform enables self-boosting reactive oxygen species generation through regulating the activity of catalase for targeted chemo/chemodynamic combination therapy, J. Colloid Interface Sci. 607 (2022) 1651-1660.

[71] Y. Liu, K. Chen, Y. Yang, P. Shi, Glucose oxidase-modified metal-organic framework for starving-enhanced chemodynamic therapy, ACS Appl. Bio Mater. 6 (2023) 857–864.

[72] T. Xue, C. Xu, Y. Wang, Y. Wang, H. Tian, Y. Zhang, Doxorubicin-loaded nanoscale metal–organic framework for tumor-targeting combined chemotherapy and chemodynamic therapy, Biomater. Sci. 2019, 7, 4615-4623.